

A 3D nanoscale optical disk memory with petabit capacity

<https://doi.org/10.1038/s41586-023-06980-y>

Miao Zhao^{1,8}, Jing Wen^{2,8}✉, Qiao Hu¹, Xunbin Wei^{3,4}, Yu-Wu Zhong⁵, Hao Ruan¹✉ & Min Gu^{6,7}✉

Received: 29 April 2023

Accepted: 14 December 2023

Published online: 21 February 2024

 Check for updates

High-capacity storage technologies are needed to meet our ever-growing data demands^{1,2}. However, data centres based on major storage technologies such as semiconductor flash devices and hard disk drives have high energy burdens, high operation costs and short lifespans^{2,3}. Optical data storage (ODS) presents a promising solution for cost-effective long-term archival data storage. Nonetheless, ODS has been limited by its low capacity and the challenge of increasing its areal density^{4,5}. Here, to address these issues, we increase the capacity of ODS to the petabit level by extending the planar recording architecture to three dimensions with hundreds of layers, meanwhile breaking the optical diffraction limit barrier of the recorded spots. We develop an optical recording medium based on a photoresist film doped with aggregation-induced emission dye, which can be optically stimulated by femtosecond laser beams. This film is highly transparent and uniform, and the aggregation-induced emission phenomenon provides the storage mechanism. It can also be inhibited by another deactivating beam, resulting in a recording spot with a super-resolution scale. This technology makes it possible to achieve exabit-level storage by stacking nanoscale disks into arrays, which is essential in big data centres with limited space.

Data storage is crucial in today's digital era, but major storage devices such as hard disk drives (HDDs)¹ and semiconductor flash devices³ have limitations in terms of cost-effectiveness, durability and sustainability^{2,5}. The optical data storage (ODS) system is a low-cost, eco-friendly and high-durability option that offers a promising solution to these problems^{1,2,4,5}. However, the current ODS capacity needs to be increased to fully meet data-centre demands, yet increasing the areal density of optical media remains a challenge⁵.

In the pursuit of enhancing the storage capacity of ODS devices, researchers have adopted two primary approaches⁵, namely, multidimensional^{6–11} and three-dimensional (3D) multilayer optical storage approaches^{11–17}. Unfortunately, both approaches have a fundamental limitation in terms of the spacing of two adjacent recorded features due to the conventional optical diffraction limit^{4,5,18}. It is challenging to realize super-resolution ODS using the current two main types of all-optical storage mechanism. Multidimensional optical storage based on the encoding of intensity and polarization states of the light utilizes the nature of plasmonic properties of metallic nanorods^{7,8} and the birefringence of a nanograting in fused quartz^{10,11}, which lack the on-off switching property like the principle of stimulated emission depletion (STED) microscopy^{19–26}. In addition, 3D multilayer optical storage on a photochromic material^{12–14}, photorefractive polymer¹⁵ or crystal¹⁶ utilizes two-photon writing, which does not have a pathway to be inhibited. Recently, the emergence of a few other approaches possessing an

on-off switching property has achieved subdiffraction bit spacing. For example, a reversibly switchable enhanced green fluorescent protein (rsEGFP) was developed to record and probe features with a subdiffraction bit spacing of about 200 nm (about $\lambda/3$, where the wavelength of the writing beam is $\lambda = 532$ nm)²⁷. Lanthanide-doped upconversion nanoparticles combined with graphene oxide have been used for optical writing with a bit spacing of about 195 nm (about $\lambda/5$, where the wavelength of the writing beam is $\lambda = 980$ nm)²⁸. However, rsEGFP has a short lifetime²⁷ such that it is not suitable for long-term ODS. Upconversion nanoparticles lack the doping homogeneity of nanoparticles spreading over photo-sensitive materials²⁸ and are thus unsuitable for volumetric ODS. Therefore, achieving nanoscale bit-wise, especially volumetric ODS that breaks the diffraction limit barrier, remains challenging^{5,18}.

Here we develop a novel ODS medium called dye-doped photoresist (DDPR) with aggregation-induced emission (AIE)²⁹ luminogens (AIE-DDPR), which has several important properties. First, for data recording, nanoscale optical writing is accomplished on the DDPR film with a triplet-triplet absorption mechanism, which efficiently deactivates polymerization via a doughnut beam^{30,31}. Second, for data retrieval, we apply an optically stimulated AIE (OS-AIE) mechanism to enhance the fluorescence emission in the region irradiated by the focused femtosecond laser beam. Similar to the STED principle, this OS-AIE phenomenon has a switching property and can be inhibited by a deactivating beam to distinguish nanoscale recording spots.

¹Photonic Integrated Circuits Center, Shanghai Institute of Optics and Fine Mechanics, Chinese Academy of Sciences, Shanghai, China. ²Engineering Research Center of Optical Instrument and Systems, Ministry of Education and Shanghai Key Lab of Modern Optical System, University of Shanghai for Science and Technology, Shanghai, China. ³Biomedical Engineering Department, Peking University, Beijing, China. ⁴School of Biomedical Engineering, Anhui Medical University, Hefei, China. ⁵Key Laboratory of Photochemistry, Beijing National Laboratory for Molecular Sciences, CAS Research Education Center for Excellence in Molecular Science, Institute of Chemistry, Chinese Academy of Sciences, Beijing, China. ⁶Institute of Photonic Chips, University of Shanghai for Science and Technology, Shanghai, China. ⁷Zhangjiang Laboratory, Shanghai, China. ⁸These authors contributed equally: Miao Zhao, Jing Wen. [✉]e-mail: jwen@usst.edu.cn; ruanhao@siom.ac.cn; gumin@usst.edu.cn

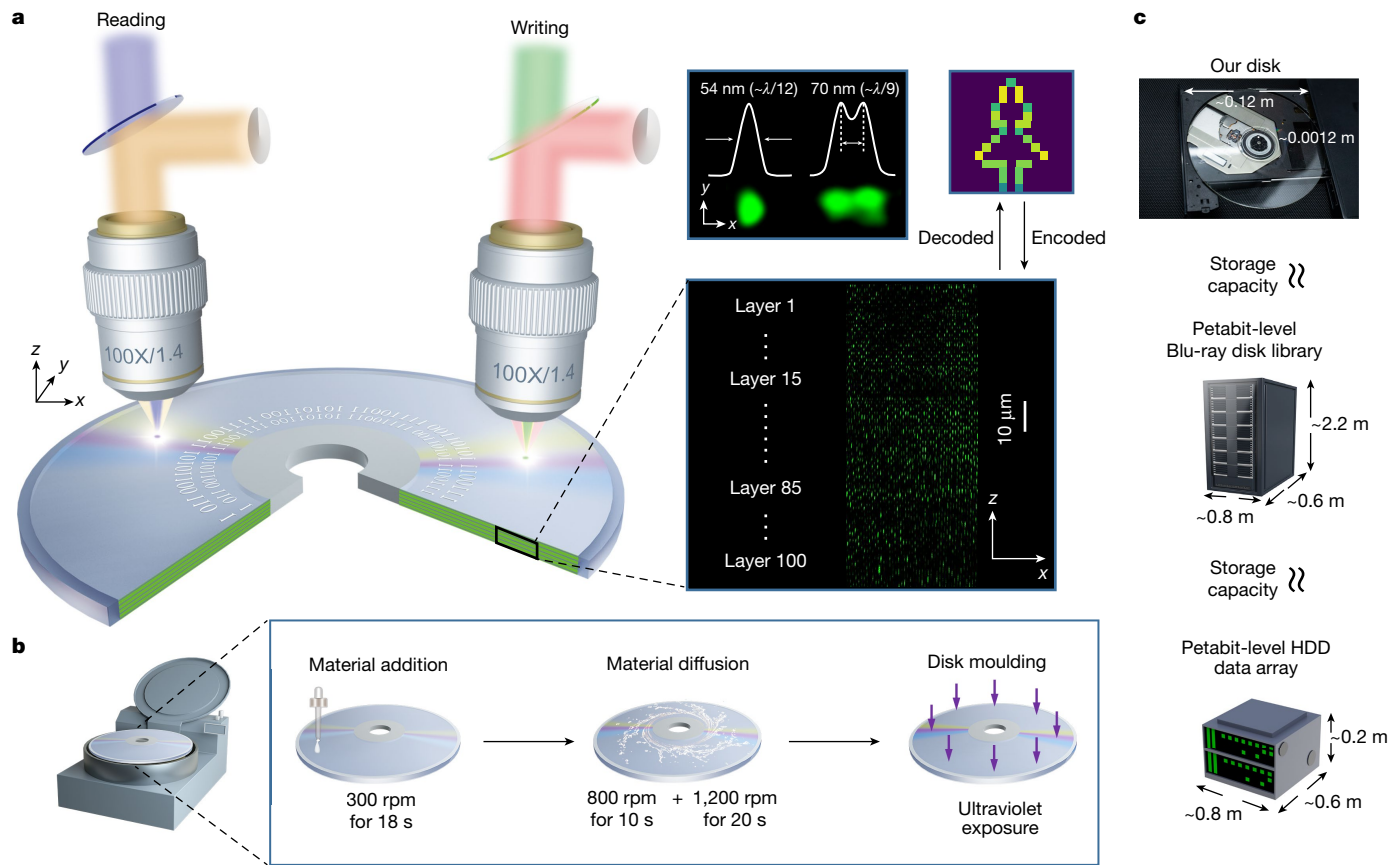


Fig. 1 | Principle of nanoscale optical writing and reading on a blank

AIE-DDPR disk and the production workflow. **a**, Dual-beam configuration for super-resolution writing and reading. A 515-nm femtosecond Gaussian laser beam and a 639-nm CW donut-shaped laser beam are used for writing. A 480-nm pulsed laser beam and a 592-nm CW laser beam are used for reading. The fluorescence image of the x - z vertical section shows nanoscale writing and reading in 100 layers. The super-resolution fluorescence image in the x - y plane shows the minimum spot size and lateral track pitch (the lateral distance between two neighbouring spots) of 54 nm (about $\lambda/12$) and 70 nm (about $\lambda/9$). **b**, Spin-coating process for material addition, material diffusion and blank-disk

moulding. AIE-DDPR in the colloidal state (Extended Data Fig. 3a) was spin-coated onto a 0.6-mm-thick transparent base disk at 300 rpm for 18 s. Next, the speed of the spin-coater was increased to 800 rpm and maintained for 10 s, and then further increased to 1,200 rpm and maintained for 20 s to evaporate all of the acetone. The resulting spin-coated disk was cured under ultraviolet illumination for 4 min. **c**, The capacity of a single 3D nanoscale disk is approximately equivalent to that of a petabit-level Blu-ray library (15.2 Pb, DA-BH7010, Hualu, China) or an HDD data array (12.64 Pb, EMC PowerVault ME5084, Dell, USA).

The AIE-DDPR recording film outperforms other optical systems and HDDs in terms of areal density (Extended Data Table 1). Our technique achieved an areal density that was approximately 125 times that of a multilayer five-dimensional optical disk based on gold nanorods⁷, 1,600 times that of a super-resolution all-optical storage based on the rsEGFP²⁷ and 24 times that of currently most advanced HDDs³².

Workflow of volumetric nanoscale optical storage

The proposed recording and retrieval processes for the ODS medium in the deep subwavelength regime are shown in Fig. 1a. For optical writing, two laser beams are focused on the recording area of the disk through the objective lens. The first beam initiates the polymerization, which is deactivated by the second beam, resulting in a record spot with subdiffractive volume size. The fluorescence signal of spots was retrieved by super-resolution optical fluorescence imaging techniques. We demonstrated the encoding and decoding processes of a tree image based on the storage workflow. The encoded information was recorded into a recording medium with 100 writing layers, the x - z vertical section of which was reconstructed from multiple x - y scans.

The workflow for producing blank disks (with no written information) made of the AIE-DDPR film is presented in Fig. 1b. The entire procedure is compatible with the standard workflow of conventional digital

versatile disc (DVD) mass production and can be completed within 6 min. A typical procedure involves spin-coating for material addition and diffusion and a process for blank-disk moulding. The ODS has a capacity of up to 1.6 Pb for a DVD-sized disk area through the recording of 100 layers on both sides of our ultrathin single disk. The ODS can store as much data as a large petabit (Pb)-level Blu-ray disk library or an HDD data array with an areal density that is 10^3 times that of a Blu-ray disk library and 24 times that of currently most advanced HDDs (Fig. 1c and Extended Data Table 1). It will thus become possible to build an exabit (Eb)-level data centre inside a room instead of a stadium-sized space by stacking 1,000 petabit-level nanoscale disks together, where each petabit-level disk is capable of replacing a conventional petabit-level Blu-ray disk library or an HDD data array, resulting in a large number of cost-effective exabit data centres.

Multilayer nanoscale writing and reading

In realizing the maximum areal density of our nanoscale ODS, we tried to write as many layers into the recording medium as possible. We successfully achieved up to 100-layer writing and reading on the proposed AIE-DDPR film, as shown in Fig. 2a (Supplementary Video 1). The writing depth in the film is 100 μ m and is limited by the working distance of the objective. We minimized the distance between neighbouring

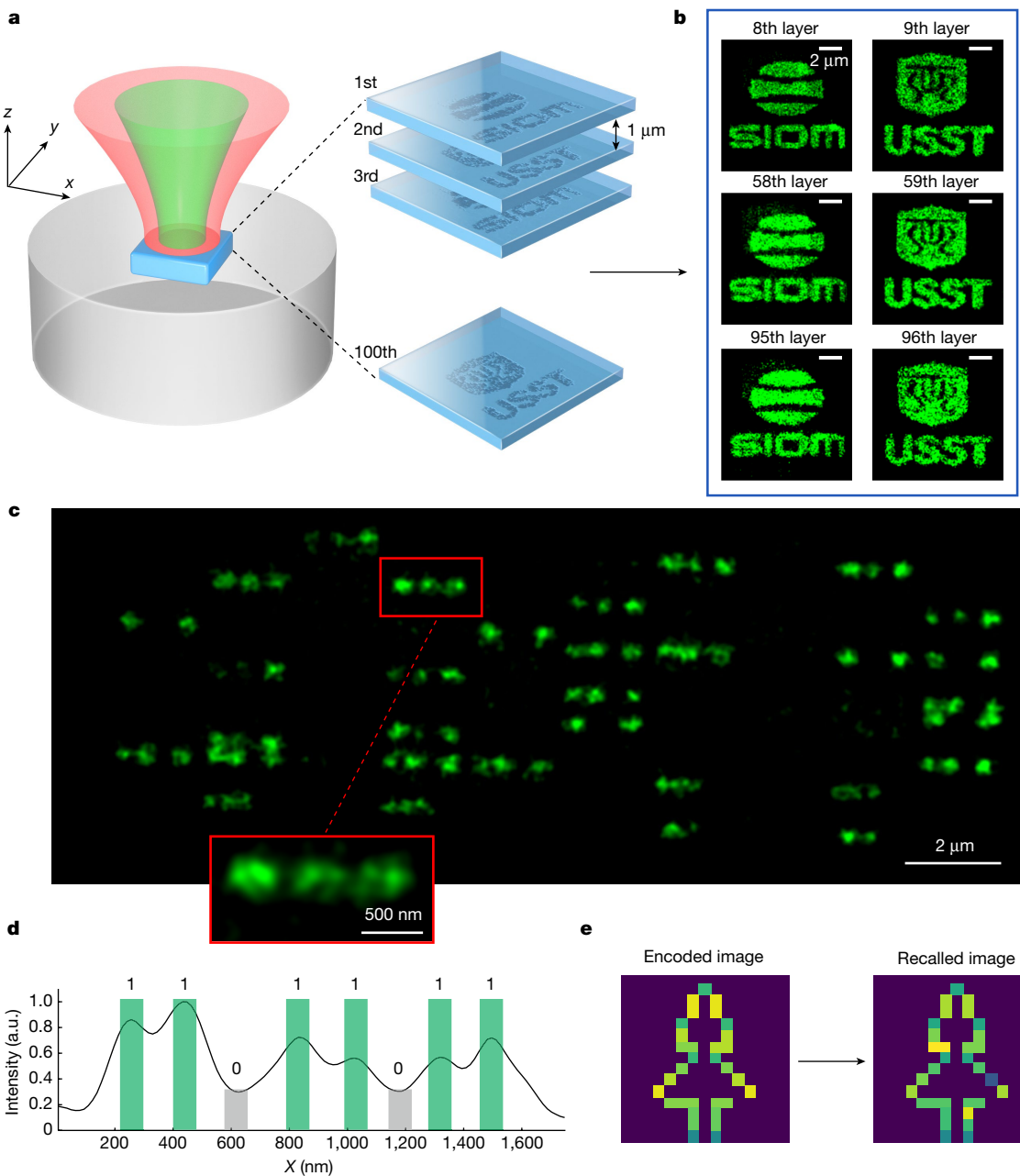


Fig. 2 | Demonstration of 100-layer volumetric nanoscale ODS and digital pattern encoding and decoding. **a**, A green 515-nm femtosecond writing laser beam and a red 639-nm CW deactivating laser beam are focused on a recording medium that comprises 100 layers with an axial layer-to-layer distance of 1 μm . **b**, Super-resolution STED-image readouts of the 8th, 9th, 58th, 59th, 95th and 96th layers. **c**, Fluorescence image of the recording layer captured by a Leica STED microscope, where the recording layer has the written information of the 8-bit binary code encoded from a tree image. Inset: a magnified view of a

specific small area. **d**, The black line represents the fluorescent intensity profile of the red box in **c**. Signal peaks indicate values of one (green bars) and signal valleys indicate values of zero (grey bars). **e**, The original tree pattern is encoded in 8-bit binary code (Extended Data Fig. 4a) for recording, and the recalled pattern is reconstructed from the 8-bit binary code (Extended Data Fig. 4b) that is extracted from the intensity profile of the STED-image readout in **c**.

layers to 1 μm to maximize the number of slices to 100. Specifically, we alternately wrote images of the institute and university badges ('SIOM' and 'USST') into the 3D volume. We found that the even and odd layers had clear alternating patterns with no cross-talk. The spatial resolution of the writing in the deeper layers was found to be comparable to that of the writing in the top layers, as evinced by the comparisons of the badges in the top (the 8th and 9th layers), middle (the 58th and 59th layers) and bottom (the 95th and 96th layers) layers shown in Fig. 2b.

In creating a prototype of a 3D nanoscale ODS device, it is crucial to establish the entire process, from encoding data (for example, images,

audio or video) to binary bits, to recording bits using the medium and retrieving the signal bit by bit (Fig. 2c), and decoding the bits to reconstruct the original digital files. The intensity profile (as shown in Fig. 2d) was obtained according to the red box shown in Fig. 2c and showed an average lateral track pitch of 180 nm. The original 8-bit image (16×16) of a tree and the corresponding recalled image are shown in Fig. 2e. Although the colour of the tree in the generated image was slightly distorted owing to the bit error rate of 0.33%, the prototype for the encoding and decoding processes based on multilayer nanoscale ODS worked well.

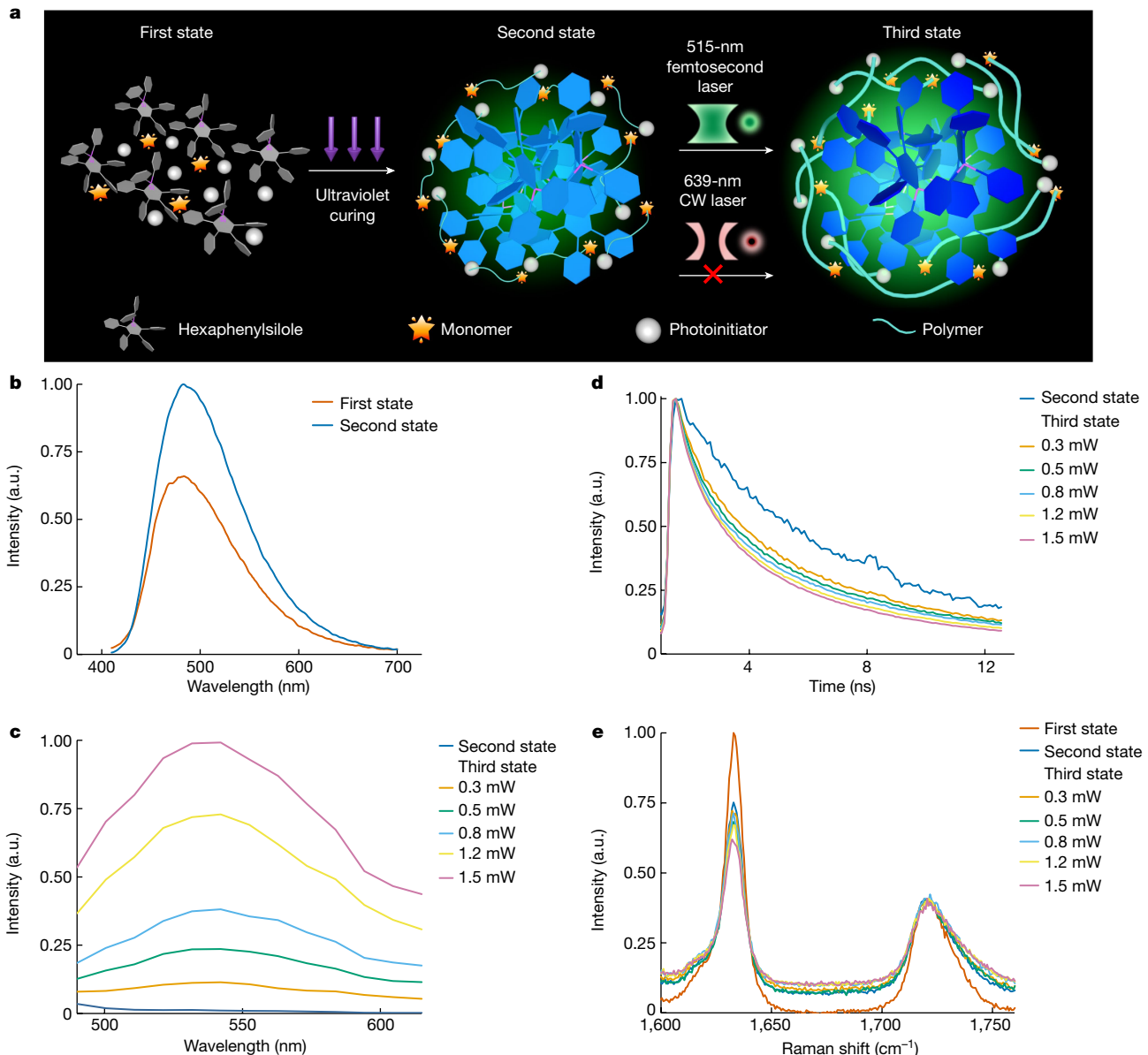


Fig. 3 | Schematic of the principle of volumetric nanoscale ODS and characterization of AIE-DDPR film. **a**, Schematic of the AIE phenomenon stimulated by a femtosecond laser beam. The transition from the second to the third state is initiated by the 515-nm femtosecond Gaussian-shaped laser beam and deactivated by the 639-nm CW doughnut-shaped laser beam. **b**, Emission

spectra of the first and second states of the film at the excitation wavelength ($\lambda = 405$ nm). **c,d**, Emission spectra (**c**) and lifetime (**d**) of the second and third states of the film at the excitation wavelength ($\lambda = 480$ nm). **e**, Raman spectroscopic measurements of the three states of the film.

Mechanism of nanoscale writing and reading

The outstanding performance of our volumetric 3D nanoscale ODS is based on the novel mechanism of nanoscale writing and reading on the AIE-DDPR film. To achieve nanoscale writing, the proposed DDPR film is composed of specific components, namely, 2-isopropylthioxanthone (ITX) initiators and dipentaerythritol penta-acrylate (DTPA) monomers. The use of ITX and DTPA, an efficient photoinitiator^{30,31} and a monomer with high photosensitivity²⁵ that has previously been used in multiphoton absorption polymerization for nanoscale photolithography^{25,30,31}, is integral to the success of the writing process. However, our writing process cannot be considered as photolithography in that it does not involve a developing step. This DDPR film alone cannot realize the function of nanoscale ODS without the following reading process.

For nanoscale reading, we incorporated hexaphenylsilole (HPS)-AIE luminogens (AIEgens) with ITX-DTPA photoresist to create an

HPS-ITX-DTPA-based AIE-DDPR film. Conventional dye molecules are often highly emissive in dilute solutions but suffer from aggregation-caused quenching in a closely packed or solid state²⁹; that is, the aggregation of luminophores has a destructive role in luminescence, making the luminophores difficult to incorporate into photoresists that are cured from solutions into cross-linked thin films for ODS. In contrast, AIEgens show extraordinary fluorescence in the aggregated and solid states²⁹. Our OS-AIE process demonstrates that the AIE phenomenon can be enhanced through optical stimulation using a highly focused femtosecond laser beam during the photochemical reaction of polymerization of HPS-ITX-DTPA. This AIE phenomenon results in a high on-off contrast ratio of the fluorescence from the region that interacts with and without the femtosecond laser beam to record information.

Our optical manipulation differs from various types of control mechanism that use electricity, magnetic fields, heat and mechanical forces²⁹

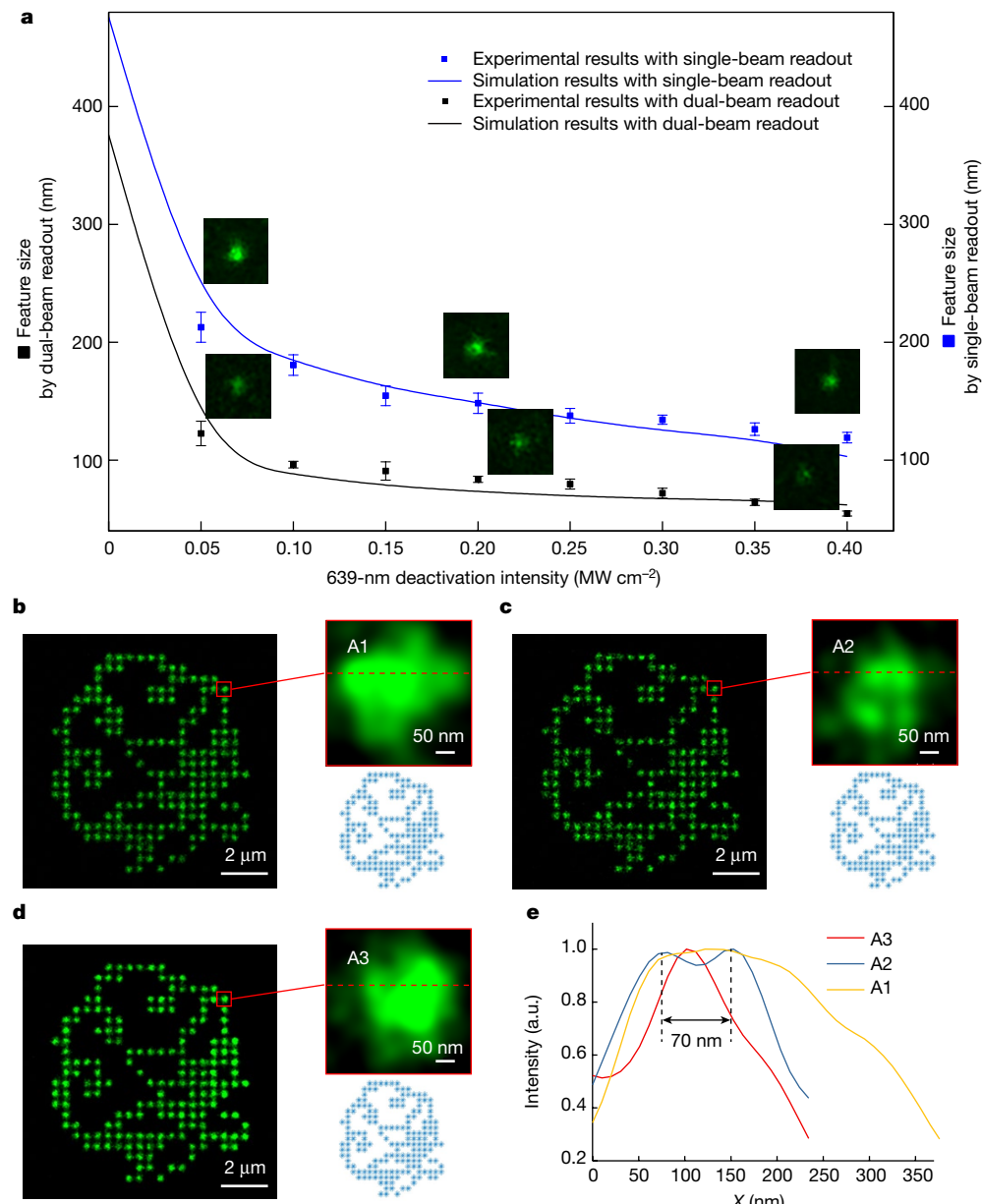


Fig. 4 | Imaging of isolated and tightly packed recording features. **a**, Suppression effect and resolution enhancement versus the intensity of the 639-nm CW deactivation beam. Insets: STED-image and confocal-image readouts of isolated recording features of various sizes. The black and blue solid lines show the numerical results of the dual-beam and single-beam readouts, respectively. The black and blue dots show the experimentally measured sizes obtained with dual-beam and single-beam imaging. The error bars indicate the standard deviations from measurements of the sizes of five different recording points using the same writing and reading parameters. **b,c**, Super-resolution STED-image readouts of the recording patterns

obtained with the writing beam of the 515-nm femtosecond laser without **(b)** and with **(c)** the 639-nm CW deactivation beam. **d**, Confocal-image readout of the recording pattern obtained under the dual-beam writing configuration. Insets: magnified images of 4×4 tightly packed recorded spots and the original lotus patterns. **e**, Intensity profiles extracted from the red dashed lines in the insets of **b–d**. In **b** and **d**, it is not possible to determine the 4×4 tightly packed recorded spots with a lateral track pitch of 70 nm. The dual-beam configuration for both writing and reading in **c** has the advantage of distinguishing the above nanoscale pattern.

to induce the AIE phenomenon. Compared with existing AIE polymers, which are typically triggered by clusterization^{33–35}, self-assembly³⁶ or changes in material composition³⁷, the precise spatial controllability of the OS-AIE process by a highly focused femtosecond laser beam that can be further effectively inhibited and deactivated by another laser beam enables us to selectively manipulate the AIE at a nanoscale. Overall, incorporating AIEgens into ITX-DTPA photoresists and utilizing the spatiotemporally controlled manipulation of this AIE-DDPR film to induce the AIE phenomenon is a promising strategy for achieving nanoscale reading in ODS systems.

Figure 3a illustrates the three distinct states of HPS-ITX-DTPA, namely, in a colloidal state, after ultraviolet light exposure and after exposure to a highly focused femtosecond laser beam. HPS-ITX-DTPA in the colloidal state (the first state) emits only a small amount of fluorescent light (Extended Data Fig. 3a). The spin-coated HPS-ITX-DTPA on the base disk is then cured with ultraviolet light, leading to a transition to the solid state and resulting in initial polymerization to a homogeneous cross-linked thin film (the second state). Subsequently, under irradiation with a 515-nm femtosecond writing laser beam, the thin film is further polymerized in the third state in which the AIE fluorescence

shows an exceptional brightness. The emission spectra of the three states are shown in Fig. 3b,c. The spectrum of the third state is red-shifted relative to that of the second state, which is probably due to the enhanced molecular coplanarization of HPS being enforced by the photopolymerization of the thin film^{38–40}. As the writing power of the 515-nm femtosecond laser beam increases, the fluorescence emissions of the third state in the reading range (490–600 nm) strengthen. This emission enhancement is due to a synergistic effect between (1) restriction of rotation of the peripheral phenyl rings, which blocks the non-radiative energy-consuming pathway, and (2) coplanarization of the peripheral phenyl rings of HPS with the silole ring, which increases the degree of conjugation and thus the radiative decay rate. The radiative and non-radiative decay rates of the controlled samples with different parameters are quantified by measuring the lifetimes (Fig. 3d) and quantum yields. In addition, Raman spectroscopic measurement (Fig. 3e) shows that the degree of polymerization increases with the writing power of the laser beam. This suggests that a higher degree of polymerization by the femtosecond laser illumination strengthens the abovementioned synergistic effect.

The whole process in Fig. 3a starts with the first 515-nm femtosecond writing laser beam triggering the transformation of the polymer from the second to the third state. Subsequently, the doughnut-shaped 639-nm continuous-wave (CW) laser beam induces the triplet–triplet absorption effect, inhibiting polymerization during the writing process and simultaneously deactivating the fluorescence enhancement of the HPS-AIEgens from the second to the third state. This ultimately results in a recorded spot of super-resolution size, which can be read by all-optically differentiating the fluorescence intensities of recorded and unrecorded areas with a high signal-to-noise ratio.

Performance for different nanoscale patterns

To obtain the maximum areal density of our nanoscale ODS, we examined the minimum size of the single recording spot and minimum track pitch. We conducted further investigations into the effect of the deactivation beam on the writing spot size, as shown in Fig. 4a, and found that the lateral size of the spot decreased as the power of the deactivation beam increased, ultimately reaching a minimum subdiffraction feature size of 54.6 ± 2.2 nm (about $\lambda/12$). In addition, confocal images (that is, single-beam readouts) of the written spots were compared with the super-resolution STED images (that is, dual-beam readouts).

A lotus flower pattern was discretized into multiple lattices of adjacent yet separated 4×4 spots, which were written by the first 515-nm femtosecond laser beam without (Fig. 4b) and with (Fig. 4c,d) the deactivation beam of the 639-nm CW laser. The results show that under a single-beam writing configuration, two neighbouring nanoscale features with a super-resolution centre-to-centre distance could not be clearly differentiated. However, under a dual-beam writing configuration, these features were closely distributed while clear individual contours were maintained. Furthermore, a comparison between the super-resolution STED-image readout (Fig. 4c) and the confocal-image readout (Fig. 4d) of the nanoscale pattern demonstrated that the dual-beam STED imaging mechanism was indispensable for accurately distinguishing tightly packed features with nanoscale track pitches. As shown in Fig. 4e, the minimum track pitch was determined to be 70 nm (about $\lambda/9$), which determines the storage capacity of the ODS system. We conclude that dual-beam configuration for both writing and reading is a requirement for nanoscale ODS.

Conclusion

Using an AIE-DDPR film as the storage medium, we developed a volumetric nanoscale ODS system that showed remarkable performance characteristics. These include a minimum spot size and a lateral track

pitch of 54 nm (about $\lambda/12$) and 70 nm (about $\lambda/9$), respectively, in each layer, in addition to a layer-to-layer axial spacing of 1 μm (about 1.6 λ). Furthermore, the ability to record up to 100 layers on both sides elevated the ODS capacity to 1.6 Pb within the area of a DVD-sized disk. These significant advantages suggest that the development of next-generation industry-oriented nanoscale ODS that is much less expensive than state-of-the-art optical disk libraries and HDD data arrays will fulfil the vast data storage requirements of the big-data era. However, although we have increased the areal density of storage substantially, further improvements in writing speed and energy efficiency are needed. This could be accomplished by using a femtosecond laser beam with a higher repetition rate and a more sensitive photoresist than those used in the current system.

Meanwhile, our research has successfully demonstrated the OS-AIE phenomenon stimulated by a femtosecond laser beam, which has important implications for the field of AIE. Our use of optical stimulation is an innovative method of spatiotemporally controlling AIE and opens up avenues for research and development in this field, particularly in terms of exploring the potential applications of OS-AIE to enhance the emission efficiency of organic light-emitting diodes for high-resolution displays and fluorescence nanoparticles for high-quality bioimaging. Furthermore, our fabrication of a nanoscale luminescent source that can be spatiotemporally controlled could lead to the discovery of materials and methods for the light sources of photonic chips.

Online content

Any methods, additional references, Nature Portfolio reporting summaries, source data, extended data, supplementary information, acknowledgements, peer review information; details of author contributions and competing interests; and statements of data and code availability are available at <https://doi.org/10.1038/s41586-023-06980-y>.

1. Reinsel, D., Gantz, J. & Rydning, J. *The Digitization of the World from Edge to Core* (IDC, 2018); <https://www.seagate.com/files/www-content/our-story/trends/files/idc-seagate-dataage-whitepaper.pdf>.
2. Sony & Panasonic. White Paper: Archival Disc Technology (2020). Sony Corporation and Panasonic Corporation <https://panasonic.cn/wp-content/uploads/2020/05/Archival-Disc-Technology-%EF%BC%9A2nd-Edition.pdf>.
3. DeBoer, S. Micron and Western Digital: the future of the National Semiconductor Technology Center. *Micron* <https://www.micron.com/about/blog/2022/august/micron-and-western-digital> (2022).
4. Sarid, D. & Schechtman, B. H. A roadmap for optical data storage applications. *Opt. Photon. News* **18**, 32–37 (2007).
5. Gu, M., Li, X. & Cao, Y. Optical storage arrays: a perspective for future big data storage. *Light Sci. Appl.* **3**, e177 (2014).
6. Ganic, D., Day, D. & Gu, M. Multi-level optical data storage in a photobleaching polymer using two-photon excitation under continuous wave illumination. *Opt. Lasers Eng.* **38**, 433–437 (2002).
7. Zijlstra, P., Chon, J. W. M. & Gu, M. Five-dimensional optical recording mediated by surface plasmons in gold nanorods. *Nature* **459**, 410–413 (2009).
8. Ouyang, X. et al. Synthetic helical dichroism for six-dimensional optical orbital angular momentum multiplexing. *Nat. Photon.* **15**, 901–907 (2021).
9. Lu, Y. et al. Tunable lifetime multiplexing using luminescent nanocrystals. *Nat. Photon.* **8**, 32–36 (2014).
10. Zhang, J., Gecevičius, M., Beresna, M. & Kazansky, P. G. Seemingly unlimited lifetime data storage in nanostructured glass. *Phys. Rev. Lett.* **112**, 033901 (2014).
11. Wang, H. et al. 100-layer error-free 5D optical data storage by ultrafast laser nanostructuring in glass. *Laser Photon. Rev.* **16**, 2100563 (2022).
12. Parthenopoulos, D. A. & Rentzepis, P. M. Three-dimensional optical storage memory. *Science* **245**, 843–845 (1989).
13. Walker, E. & Rentzepis, P. M. Two-photon technology a new dimension. *Nat. Photon.* **2**, 406–408 (2008).
14. Walker, E., Dvornikov, A., Coblenz, K., Esener, S. & Rentzepis, P. Toward terabyte two-photon 3D disk. *Opt. Express* **15**, 12264–12276 (2007).
15. Day, D., Gu, M. & Smallridge, A. Use of two-photon excitation for erasable–rewritable three-dimensional bit optical data storage in a photorefractive polymer. *Opt. Lett.* **24**, 948–950 (1999).
16. Kawata, Y., Ishitobi, H. & Kawata, S. Use of two-photon absorption in a photorefractive crystal for three-dimensional optical memory. *Opt. Lett.* **23**, 756–758 (1998).
17. Kalpalalli, D. L. N. et al. Ultra-high density optical data storage in common transparent plastics. *Sci. Rep.* **6**, 26163 (2016).
18. Gu, M., Zhang, Q. & Lamon, S. Nanomaterials for optical data storage. *Nat. Rev. Mater.* **1**, 16070 (2016).

19. Hell, S. W. & Wichmann, J. Breaking the diffraction resolution limit by stimulated emission: stimulated-emission-depletion fluorescence microscopy. *Opt. Lett.* **19**, 780 (1994).

20. Scott, T. F., Kowalski, B. A., Sullivan, A. C., Bowman, C. N. & McLeod, R. R. Two-color single-photon photoinitiation and photoinhibition for subdiffraction photolithography. *Science* **324**, 913–917 (2009).

21. Li, L., Gattass, R. R., Gershoren, E., Hwang, H. & Fourkas, J. T. Achieving $\lambda/20$ resolution by one-color initiation and deactivation of polymerization. *Science* **324**, 910–913 (2009).

22. Andrew, T. L., Tsai, H.-Y. & Menon, R. Confining light to deep subwavelength dimensions to enable optical nanopatterning. *Science* **324**, 917–921 (2009).

23. Fischer, J. & Wegener, M. Ultrafast polymerization Inhibition by stimulated emission depletion for three-dimensional nanolithography. *Adv. Opt. Mater.* **24**, OP65–OP69 (2012).

24. Fischer, J. & Wegener, M. Three-dimensional direct laser writing inspired by stimulated-emission-depletion microscopy. *Opt. Mater. Express* **1**, 614–624 (2011).

25. Gan, Z., Cao, Y., Evans, R. A. & Gu, M. Three-dimensional deep sub-diffraction optical beam lithography with 9nm feature size. *Nat. Commun.* **4**, 2061 (2013).

26. Chen, X. & Gu, M. Two-beam ultrafast laser scribing of graphene patterns with 90-nm subdiffraction feature size. *Ultrafast Sci.* **2022**, 0001 (2022).

27. Grotjohann, T. et al. Diffraction-unlimited all-optical imaging and writing with a photochromic GFP. *Nature* **478**, 204–208 (2011).

28. Lamon, S., Wu, Y., Zhang, Q., Liu, X. & Gu, M. Nanoscale optical writing through upconversion resonance energy transfer. *Sci. Adv.* **7**, eabe2209 (2021).

29. Hu, R., Leung, N. L. C. & Tang, B. Z. Aie macromolecules: syntheses, structures and functionalities. *Chem. Soc. Rev.* **43**, 4494–4562 (2014).

30. Liaros, N. et al. Elucidating complex triplet-state dynamics in the model system isopropylthioxanthone. *iScience* **25**, 103600 (2022).

31. Fischer, J., Freymann, G. V. & Wegener, M. The materials challenge in diffraction-unlimited direct-laser-writing optical lithography. *Adv. Mater.* **22**, 3578–3582 (2010).

32. Gardner, T. Has HDD areal density stalled? *StorageNewsletter* <https://www.storagenewsletter.com/2022/04/19/has-hdd-areal-density-stalled> (2022).

33. Zhang, H. et al. Clusterization-triggered emission: uncommon luminescence from common materials. *Mater. Today* **32**, 275–292 (2020).

34. Song, B. et al. Facile conversion of water to functional molecules and cross-linked polymeric films with efficient clusteroluminescence. *Nat. Commun.* **14**, 3115 (2023).

35. Tang, S. et al. Nonconventional luminophores: characteristics, advancements and perspectives. *Chem. Soc. Rev.* **50**, 12616–12655 (2021).

36. Ma, C. et al. A biocompatible cross-linked fluorescent polymer prepared via ring-opening PEGylation of 4-arm PEG-amine, itaconic anhydride, and an AIE monomer. *Polym. Chem.* **6**, 3634–3640 (2015).

37. Zhao, D. et al. Photopolymerization with AIE dyes for solid-state luminophores. *Polym. Chem.* **11**, 1589–1596 (2020).

38. Zhang, T. et al. Aggregation effects on the optical emission of 1,1,2,3,4,5-hexaphenylsilole (HPS): a QM/MM study. *J. Phys. Chem. A* **118**, 9094–9104 (2014).

39. Gu, X. et al. Polymorphism-dependent emission for dip(*p*-methoxyphenyl)dibenzofulvene and analogues: optical waveguide/amplified spontaneous emission behaviors. *Adv. Funct. Mater.* **22**, 4862–4872 (2012).

40. Sonoda, Y., Tsuzuki, S., Goto, M., Tohnai, N. & Yoshida, M. Fluorescence spectroscopic properties of nitro-substituted diphenylpolyenes: effects of intramolecular planarization and intermolecular interactions in crystals. *J. Phys. Chem. A* **114**, 172–182 (2010).

Publisher's note Springer Nature remains neutral with regard to jurisdictional claims in published maps and institutional affiliations.

Springer Nature or its licensor (e.g. a society or other partner) holds exclusive rights to this article under a publishing agreement with the author(s) or other rightsholder(s); author self-archiving of the accepted manuscript version of this article is solely governed by the terms of such publishing agreement and applicable law.

© The Author(s), under exclusive licence to Springer Nature Limited 2024

Methods

Preparation and composition of AIE-DDPR

All of the reagents and solvents were of reagent grade and used without further purification. Irgacure ITX (Ryoji) was used as the photoinitiator, DTPA (≤ 650 ppm 4-methoxyphenol; Rhawn) was used as the monomer for photopolymerization and HPS was used as the AIE fluorophore (Sigma-Aldrich). AIE-DDPR was prepared as follows.

Irgacure ITX (20.0 mg, 78.63 μmol) and HPS (10 mg, 18.56 μmol) were added to DTPA (1 ml), and the resulting solution was treated with acetone (12 ml). The resulting mixture was vigorously stirred on a hot plate at 50 °C for 1 h to afford a solution, which was then heated in an oven at 60 °C for 24 h to remove residual acetone. The final formulation of the photoresist included 1.69 wt% Irgacure ITX, 0.84 wt% HPS and 97.47 wt% DTPA.

Configuration for dual-beam volumetric nanoscale writing

The optical configuration for dual-beam volumetric nanoscale writing (Extended Data Fig. 1) contained two laser beams: a 515-nm femtosecond Gaussian-shaped writing laser beam (ACL-AFS-515-CUS, Acculasers) with a repetition rate of 42 MHz, a pulse width of 180 fs and a peak intensity of 2.14 GW cm^{-2} (corresponding to a time-averaged power of 0.17 mW and an energy per bit of information of 17 μJ in the focal plane of the objective), and a linearly polarized 639-nm CW doughnut-shaped deactivating laser beam (MR-FN-639, Hefei Max-ray Photonics). A minimum recording resolution of 54.6 nm was achieved when the deactivating beam intensity was 0.4 MW cm^{-2} (corresponding to a time-averaged writing power of 36.4 mW and an energy per bit of information of 3.64 mJ in the focal plane of the objective).

The above-described configuration was used as follows. First, the two beams were collimated and expanded via lenses (L1–L4) and pinholes (PH1 and PH2). Next, a half-wave plate (WPH10M-633, Thorlabs) and a quarter-wave plate (WPQ10M-633, Thorlabs) in the path of the 639-nm CW deactivating laser beam converted it from a linearly polarized beam to a circularly polarized beam. Subsequently, the 515-nm femtosecond writing laser beam (passed through an electrical shutter (model 76992, Newport)) and the 639-nm CW deactivating beam were reflected by dichroic mirrors DC1 and DC2 (ZT375/514/594rpc and ZT405/488/532/640rpc-XT, Chroma), respectively, and then focused by an oil-immersion objective (UPlanSApo, Olympus; $\times 100$, numerical aperture 1.4) onto the sample surface. The 639-nm CW laser beam was scanned over the labelled spot written by the 515-nm femtosecond laser beam to achieve fast and precise alignment of the two beams before the writing process. The fluorescence signal generated by the 515-nm and 639-nm laser beams was transmitted through DC1 and DC2 and split into two paths by a beam-splitter (BS013, Thorlabs). One path was collected by a spectrometer (Aurora4000-E, Cnilaser). The coincidence degree of the solid 515-nm and doughnut 639-nm laser beams in three dimensions affected the spatial resolution of the written spot. The 3D coincidence of the two beams was adjusted and continued until the beams were coincident, and then a vortex-phase plate (VPP-1a, RPC Photonics) was added into the optical path to ensure that the 639-nm CW laser beam exhibited a high-quality doughnut shape. The vortex-phase plate generated a spiral optical distribution in the beam cross-section along the azimuthal direction to the optical axis. The optical intensity was zero at the centre, owing to the phase singularity. Afterwards, the writing process began. In the other path, the fabrication process was simultaneously imaged by a tube lens (L6) with a focal length of $f = 180$ mm to a charge-coupled device (CN3-U3-31S4M-CS, FLIR). The sample was fixed onto a high-speed motorized x - y - z piezoelectric scanning stage (P-563.3CD, PI). A bespoke programme was used to synchronize the timeslot of the pulse laser beam, the electronic shutter and the movement of the piezoelectric stage. The pixel dwell time (that is, the light exposure time) was 100 ms, which involved 4.2×10^6 pulses (generated by the opening of the electronic shutter).

The piezoelectric stage (scanning speed 200 $\mu\text{m s}^{-1}$) took 0.35 ms to move from one pixel to the next (with simultaneous shut-down of the electronic shutter).

Configuration for dual-beam super-resolution reading

For data retrieval, we used a 480-nm pulsed laser beam (repetition rate 80 MHz; pulse width 5 ps) for excitation and a 592-nm CW laser beam for depletion. The excitation light source of the STED microscope (TCS SP8 STED 3X, Leica) had a wavelength range of 470–700 nm and this probably efficiently excited the fluorescence of AIEgens. The depletion light-source wavelength could be selected to be 561 nm, 592 nm (which we used) or 660 nm, which probably lie at the end of the emission spectra of AIEgens. Extended Data Fig. 2 compares the readout images of ODS mediums doped with tetraphenylethene (Extended Data Fig. 2a), no AIEgens (Extended Data Fig. 2b) and HPS (Extended Data Fig. 2c). The fluorescence intensities of the recording media based on tetraphenylethene (Extended Data Fig. 2d) and no AIEgens (Extended Data Fig. 2e) were at the same level and were much lower than those of the medium based on HPS (Extended Data Fig. 2f). The excitation and emission spectra of tetraphenylethene did not match the wavelength range of our STED microscope. We found that the main component of the luminescence of the AIE-DDPR film was from HPS and was not due to the clusteroluminescence of the film. The fluorescence signal of spots at 490–580 nm was collected by an objective (HC PL APO $\times 100/1.40$ OIL STED WHITE, Leica) installed on the microscope. Super-resolution scanning images were recorded at a data rate of 400 Hz. In Fig. 1a, the bit voxel size is 29 nm \times 29 nm \times 1 μm ; the logical and physical sizes of the magnified x - y slice are 2,200 \times 2,200 and 63.46 $\mu\text{m} \times$ 63.46 μm , respectively. The vertical image section that has 100 writing layers was reconstructed from multiple x - y scans. In Fig. 2b,c, the bit voxel size is 15 nm \times 15 nm \times 100 nm; and the logical and physical sizes of the magnified x - y slice are 2,704 \times 2,704 and 39.68 $\mu\text{m} \times$ 39.68 μm , respectively. In Extended Data Fig. 7a, the bit voxel size is 17 nm \times 17 nm \times 40 nm; and the logical and physical sizes of the magnified x - y slice are 2,504 \times 2,504 and 41.52 $\mu\text{m} \times$ 41.52 μm , respectively. In Fig. 4a, the single-beam confocal-image and dual-beam STED-image readout have a bit voxel size of 7 nm \times 7 nm \times 30 nm; and the logical and physical sizes of the magnified x - y slice are 4,800 \times 4,800 and 33.21 $\mu\text{m} \times$ 33.21 μm , respectively. In Fig. 4b–d, the bit voxel size is 10 nm \times 10 nm \times 20 nm; and the logical and physical sizes of the magnified x - y slice are 3,000 \times 3,000 and 29.81 $\mu\text{m} \times$ 29.81 μm , respectively. In Extended Data Fig. 7c,d, the bit voxel size is 18 nm \times 18 nm \times 20 nm; and the logical and physical sizes of the magnified x - y slice are 2,600 \times 2,600 and 47.83 $\mu\text{m} \times$ 47.83 μm , respectively.

Homogeneity, transmittance and thickness of an AIE-DDPR film

The ultrahigh homogeneity and transparency of the film indicate the film's suitability as a multilayer recording medium. The good solubility of HPS-AIEgens in organic solvents enables the formation of highly uniform AIE-DDPR films. The transmission electron microscopy images showed that the cured AIE-DDPR film was homogeneous and smooth (Extended Data Fig. 2g,h), which is a prerequisite for extremely high-spatial-resolution super-resolution writing and reading. Moreover, a prerequisite for multilayer storage is a sufficiently transparent recording medium and volumetric recording into many layers is possible if a film shows ultrahigh transmittance. Both AIE-DDPR in the colloidal state and the cured AIE-DDPR film are transparent under white-light illumination and radiate fluorescent light under ultraviolet illumination (Extended Data Fig. 3a,b). A disk treated with the AIE-DDPR film is as transparent as a base disk comprising only pure substrate (Extended Data Fig. 3c,d). We examined and compared the transmittance of the cured AIE-DDPR film and that of the pure silica substrate (Extended Data Fig. 2i). The transmittance of the cured AIE-DDPR film remained as high as 95–97% at a wavelength of 500–700 nm. The thickness of the AIE-DDPR film on a base disk was 158.13 ± 0.19 μm .

Optimization of layer spacing and layer numbers

The working distance of the objective (UPlanSApo, Olympus; $\times 100$, numerical aperture 1.4) for writing was 130 μm , which limited the maximum writing depth. We found that the effective written depth was 100 μm . The 30- μm difference might have represented the written depth of the first recording layer from the top surface of the AIE-DDPR film. We optimized the layer spacing, and Extended Data Fig. 3e–g shows that there was obvious cross-talk of the signal between neighbouring layers with layer spacings of 0.5 μm and 0.7 μm . It is clearly seen that the volumetric writing was limited to 1 μm per layer with a maximum of 100 layers.

Detailed process of encoding and decoding

We encoded a tree image to an 8-bit binary code (Extended Data Fig. 4a) and recorded the image in the medium. Fluorescence images of the recorded patterns were then captured using a Leica STED microscope (Fig. 2c) and converted to binary bits (Extended Data Fig. 4b). These binary bits were then used to reconstruct the recalled image.

Mechanism of nanoscale writing and fundamental kinetic modelling

The ITX polymerization deactivation process operates through a triplet–triplet absorption mechanism, rather than the commonly used STED mechanism^{30,31,41–43}. The triplet–triplet absorption phenomenon⁴³ is stimulated by a deactivating beam of a 639-nm CW laser and is accompanied by molecules transitioning from the lowest triplet state T_1 to the excited triplet state T_n . This transition reduces the number of molecules in state T_1 and thus inhibits radical formation and contributes to photoresist depolymerization, resulting in nanoscale writing. The mechanism is elucidated by a schematic Jablonski diagram of ITX photoinitiators (Extended Data Fig. 5a). Subsequently, a subdiffractive recorded spot is written on the AIE-DDPR film (Extended Data Fig. 5b). The differential equations of fundamental kinetic modelling describe the dynamic photo-physical and photochemical processes involved in polymerization and depolymerization. These processes include photoinitiation, deactivation of photoinitiation, chain propagation, chain termination and radical polymerization. The set of kinetic rate equations is as follows.

$$\frac{dP_0(r, t)}{dt} = -\sigma_E I_E(r, t)^2 (P_0(r, t) - P_1(r, t)) + k_i P_1(r, t) + k_q T_1(r, t) + k_s T_n(r, t) \quad (1)$$

$$\frac{dP_1(r, t)}{dt} = \sigma_E I_E(r, t)^2 (P_0(r, t) - P_1(r, t)) - k_i P_1(r, t) - k_{\text{ISC}} P_1(r, t) \quad (2)$$

$$\frac{dT_1(r, t)}{dt} = k_{\text{ISC}} P_1(r, t) - k_q T_1(r, t) - \sigma_D I_D(r) (T_1(r, t) - T_n(r, t)) - k_d T_1(r, t) \quad (3)$$

$$\frac{dT_n(r, t)}{dt} = \sigma_D I_D(r) (T_1(r, t) - T_n(r, t)) - k_s T_n(r, t) \quad (4)$$

$$\frac{dP_2(r, t)}{dt} = k_d T_1(r, t) - k_i P_2(r, t) M(r, t) - k_t P_3(r, t) P_2(r, t) \quad (5)$$

$$\frac{dP_3(r, t)}{dt} = k_i P_2(r, t) M(r, t) - k_p P_3(r, t) M(r, t) - k_t (P_3(r, t) + P_2(r, t)) P_3(r, t) \quad (6)$$

$$\frac{dM(r, t)}{dt} = -k_p P_3(r, t) M(r, t) - k_i P_2(r, t) M(r, t) \quad (7)$$

1. In the above equations, P_0 and P_1 are the concentrations of the photoinitiators (photosensitizer) in the S_0 state (comprising the electronic ground level and the vibrationally excited level) and the excited electronic S_1 state (comprising the vibrationally relaxed level and the hot level), respectively; T_1 and T_n are the concentrations of the photoinitiators (photosensitizer) in the lowest triplet state T_1 and the excited triplet state T_n , respectively; P_2 , P_3 and M are the densities of primary radicals, propagating radicals, and monomers; and $(1 - M)$ is the photopolymerization conversion rate, which is the proportion (%) of monomers in the focal region that have been polymerized. The region where $(1 - M)$ is higher than a specific threshold (42% in this study) becomes a recording spot on the substrate.

2. The 515-nm femtosecond laser beam initiates the polymerization of the AIE-DDPR film via two-photon absorption with reaction time t . The intensity of the laser beam is radially symmetric with radius axis r . The photoinitiators are driven from the electronic ground state S_0 to the excited electronic state S_1 via two-photon absorption with rate constant $\sigma_E I_E^2$, where I_E is the photon flux of the 515-nm femtosecond laser beam during excitation and σ_E is the corresponding two-photon absorption cross-section. The molecules in the S_1 state relax to the vibrationally relaxed electronically excited state via intramolecular vibrational redistribution. Excited molecules in the S_1 state then either decay to the S_0 state by spontaneous fluorescence with rate constant k_1 (described by $k_1 P_1$), undergo non-radiative relaxation (ignored in the formula) or undergo intersystem crossing (ISC) to the triplet state T_1 with rate constant k_{ISC} . Molecules in the T_1 state can follow one of three main pathways. One pathway involves participating in chemical reactions, that is, radical generation and polymerization initiation, the characteristic parameters for which are represented in the next note (3). The second pathway involves relaxation to the S_0 state by phosphorescent emission with rate constant k_q (described by $k_q T_1$). The third pathway involves some of the molecules being excited from the lowest triplet state T_1 to a higher triplet state T_n (that is, undergoing triplet–triplet absorption)³⁴ by the deactivating optical beam with a rate constant $\sigma_D I_D$, where I_D is the photon flux of the deactivating optical beam of the 639-nm CW laser beam and σ_D is the corresponding absorption cross-section. If I_D increases gradually, the rate constant $\sigma_D I_D$ increases, which indicates that there is an increase in the number of molecules following the third pathway, that is, in the number of molecules that are excited from the T_1 state to the T_n state. Thus, there is a decrease in the number of molecules following the first pathway, that is, in the number of molecules contributing to the polymerization initiation. This explains why the lateral size of the spot decreased as the power of the deactivation beam increased, as demonstrated in Fig. 4a. It was proposed that the T_n state undergoes reverse ISC to an excited singlet state S_n (ref. 34). However, it may relax rapidly to the S_1 state and thus induce repopulation of the T_1 state, due to the high triplet quantum yield of S_1 , thereby markedly weakening the deactivation process³⁰. Compared with the above process, the T_n state has a higher probability of undergoing instantaneous reverse ISC to a highly vibrationally excited level of the S_0 state with rate constant k_s (described by $k_s T_n$), which relaxes via intramolecular vibrational redistribution³⁰.

3. ITX is a Norrish type II initiator, as it generates only one efficient primary radical with rate constant k_d (described by $k_d T_1$); ITX generates another radical that is weak and thus not considered⁴⁴. k_i is the kinetic conversion rate of propagating radicals evolved from the reaction between initiator radicals and monomers. k_t is the termination rate of the initiator and propagating radicals. k_p is the kinetic conversion rate of the propagating radicals involved in chain propagation^{44–46}.

4. The parameters in the equations take the following values. The two-photon absorption cross-section is $\sigma_{E, \lambda=515\text{nm}} = 5 \text{ GM}$ (1 GM = $1 \times 10^{-50} \text{ cm}^4 \text{ per photon}$)⁴¹. The single-photon absorption cross-section $\sigma_{D, \lambda=639\text{nm}} = 1.15 \times 10^{-16} \text{ cm}^2$ is calculated from the molar extinction coefficient⁴⁷ $\epsilon_D = 3 \times 10^4 \text{ l mol}^{-1} \text{ cm}^{-1}$. $k_1 = 1/\tau_f = 4.3 \times 10^8 \text{ s}^{-1}$ is calculated

from the fluorescence decay time of the S_1 state $\tau_f = 2.3$ ns (ref. 31). $k_q = 1/\tau_q = 8.3$ s $^{-1}$ is calculated from the phosphorescence decay time of the T_1 state $\tau_q = 120$ ms (ref. 41). $k_{ISC} = 2.4 \times 10^9$ s $^{-1}$ (ref. 31). The following three parameters are obtained from the literature^{45,46}: $k_i = 9.6 \times 10^4$ s $^{-1}$, $k_t = 5 \times 10^3$ s $^{-1}$ and $k_p = 5.5 \times 10^3$ s $^{-1}$. The following two parameters are fitted numerically to the experimental data: $k_s = 5 \times 10^4$ s $^{-1}$ and $k_d = 2 \times 10^4$ s $^{-1}$. The expressions of the excitation and the deactivating beams are as follows: $I_E(r, t) = \Phi_{max} \exp\left(\frac{-2r^2}{w_0^2}\right) \exp\left(\frac{-2(t-2t_0)^2}{t_0^2}\right)$, where Φ_{max} is the peak number of excitation photons per area per unit time, which is calculated from the peak intensity I_{max} of the excitation beam (2.14 GW cm $^{-2}$) in the focal plane of the objective. That is, $\Phi_{max} = \frac{I_{max}}{h\nu_E} = 5.55 \times 10^{27}$ (cm 2 s) $^{-1}$. The beam width and the pulse width of the excitation laser beam are

$$w_0 = 350 \text{ nm and } t_0 = 180 \text{ fs, respectively. } I_D(r) = \frac{2\Phi_{av} \left[\frac{4r^2}{\pi w_1^4} \exp\left(\frac{-2r^2}{w_1^2}\right) \right] \Phi_{av}}{\left[\frac{4r^2}{\pi w_1^4} \exp\left(\frac{-2r^2}{w_1^2}\right) \right]_{max}}.$$

is the average number of deactivating photons per area per unit time, which is calculated from the average intensity I_{av} of the deactivating beam (0.4 MW cm $^{-2}$ for a spot size of 54.6 nm) in the focal plane of the objective. $\Phi_{av} = \frac{I_{av}}{h\nu_D} = 1.3 \times 10^{24}$ (cm 2 s) $^{-1}$. The width of the deactivating laser beam $w_1 = 850$ nm. The Planck constant is represented by $h = 6.62176 \times 10^{-34}$ J s. The frequencies of the laser beams are $\nu_E = 5.82 \times 10^{14}$ Hz and $\nu_D = 4.69 \times 10^{14}$ Hz, respectively.

5. Simulated profiles of photopolymerization conversion rate versus various deactivating intensities are shown in Extended Data Fig. 5c. However, these physical sizes are not the final feature sizes observed by STED microscopy, because experimentally observed sizes are affected by the resolution of a STED microscope. That is, patterns with features smaller than the resolution cannot be determined clearly. The determination of final feature size is discussed in the next section.

Observation of feature size of a nanoscale writing spot by STED microscopy

The final feature size of a nanoscale writing spot observed by STED microscopy is a convolution between the solution of the above set of kinetic rate equations (the size of the physical writing spots) and the point-spread function (PSF) of the STED microscope that is used, that is

$$\text{Observed feature size} = \text{Physical size} \otimes \text{Detection PSF.} \quad (8)$$

Similarly, the PSF of a STED microscope can be obtained by solving the kinetic rate equations for the polymerization film excited by a 480-nm pulsed laser beam. The depletion beam was a 592-nm CW laser beam, and the depletion effect can be derived analytically, as follows:

$$\frac{dn(r, t)}{dt} = -k_f n(r, t) - \sigma I_{STED}(r) n(r, t) \quad (9)$$

where $n(r, t)$ is the number of molecules in the excited electronic state, k_f is the fluorescence decay rate, σ is the stimulated emission cross-section, and $I_{STED}(r)$ is the spatially dependent photon flux of the depletion beam (that is, the number of photons per area per unit time). $k_f = 1/\tau_f$, where τ_f is the fluorescence lifetime. Thus, the solution of equation (9) is

$$n(r, t) = n_0 e^{-(k_f + \sigma I_{STED}(r))t} \quad (10)$$

where n_0 is the total number of fluorophores. Thus, the change in the number of fluorescent photons emitted versus time is described by the following differential equation:

$$\frac{dN_f(r, t)}{dt} = k_f n(r, t) \quad (11)$$

The number of fluorescent photons can be obtained by solving equation (11), which gives:

$$N_f(r, t) = n_0 \frac{k_f}{k_f + \sigma I_{STED}(r)} (1 - e^{-(k_f + \sigma I_{STED}(r))t}) \quad (12)$$

The detected fluorescent spot size $h_f(r)$ (that is, PSF) is the product of the excitation beam distribution $R_f(r)$ and the spatially varying fluorescence emission probability $\eta(r)$, that is

$$h_f(r) = R_f(r) \eta(r) = R_f(r) \lim_{t \rightarrow \infty} (N_f(r, t)/n_0) = R_f(r) \frac{k_f}{k_f + \sigma I_{STED}(r)} \quad (13)$$

The parameters we used in the simulation were $\sigma = 7 \times 10^{-16}$ cm 2 , $\tau_f = 1$ ns and $t \rightarrow \infty$ for the CW depletion beam. The average power density in the focal plane was 10.7 MW cm $^{-2}$. By following the above steps, we obtained the simulation results in Extended Data Fig. 5d–g, which are consistent with the findings presented in Fig. 4b–e, further corroborating the accuracy and validity of the results.

Characterization of photoluminescence quantum yield

The quantum yields (QYs) of the recorded areas at different writing powers of the 515-nm femtosecond laser beam (that is, the third state) are summarized in Extended Data Table 2. We used Williams' comparative method⁴⁸ to characterize the absolute QY of an AIE-DDPR film before and after its interaction with the 515-nm femtosecond laser beam. The thin film of Ru(bpy) $_3$ Cl $_2$ was used as a standard sample and prepared from the solution in methanol with a concentration of 5×10^{-3} M by spin-coating. Its absolute emission QY was 7.3%, which was obtained on Quantaurus-QY spectrometer (C11347, Hamamatsu). Its property is depicted in Extended Data Fig. 6a–c. The absorbance of the standard sample (A_s) and the test sample of our AIE-DDPR film (A_T) at an excitation wavelength $\lambda = 480$ nm and their photoluminescence spectra were obtained by scanning the samples utilizing the imaging platform (STELLARIS 8 STED FALCON, Leica). The excitation laser beam was focused by an objective (HC PL APO $\times 100/1.40$ OIL STED WHITE, Leica) to the sample. Subsequently, the fluorescence emitted from a sample (the standard sample or the test sample) was collected by the same objective and spectrally filtered by a prism and a slit before the detection camera, which recorded its photoluminescence spectrum. The integrated fluorescence intensities of the test sample (I_T) and the standard sample (I_s) were calculated from their photoluminescence spectra (Extended Data Fig. 6d). The absolute QYs of the test sample were calculated as follows:

$$\text{QY}_T = \text{QY}_S \left(\frac{I_T \times A_s}{I_s \times A_T} \right) \quad (14)$$

where the subscripts S and T denote the standard and the test samples, respectively, I is the integrated fluorescence intensity, and A is the absorbance at the excitation wavelength ($\lambda = 480$ nm).

Measurement of on–off contrast of fluorescence

An elevated on–off contrast ratio of the fluorescence emissions from HPS–ITX–DTPA in the third and second states reaches 60:1. We adopted confocal microscopy to continuously probe the fluorescence emitted by recorded spots at a scanning speed of 3.4 s per frame (that is, one-time data writing and multiple-time data reading) and thereby observed the dynamic variance in the readout (Extended Data Fig. 6e–h). The decreasing trend in the on–off contrast in Extended Data Fig. 6e indicates the occurrence of photobleaching. Subsequent to the initiation of excitation, the on–off contrast reached 60:1 at 7 min (Extended Data Fig. 6f), decayed to 33:1 (a decrease of approximately 50%) at 27 min (Extended Data Fig. 6g), and remained largely unchanged from 100 to 134 min (that is, from the 1,765th to the 2,365th reading) and as

high as 20.5:1 (Extended Data Fig. 6e,h). This means that the ODS of the AIE-DDPR medium could support up to 2,365 readings.

Characterization of aggregation size, lifetime, degree of polymerization, and radiative and non-radiative decay rates of the AIE-DDPR film

As the power of the writing laser beam decreased, the aggregation size and fluorescence intensity decreased (Extended Data Fig. 7a). Fluorescence and optical image profiles are profiles of grey values extracted from the fluorescence and optical images in the area of the recorded spots at different writing powers of the 515-nm femtosecond laser beam. We posited that although subdiffractive spots can be recorded by reducing the writing power of a single laser beam to below a certain threshold, the luminescent nanofeatures of the spots might not be optically clarified, owing to the ultralow fluorescence signal. This highlights the fact that high-fluorescence on-off contrast and super-resolution of a recorded spot are trade-off parameters in single-beam writing. However, a dual-beam writing configuration can circumvent the aforementioned trade-off, and thus this configuration was used not only for nanoscale writing but also for efficient retrieval of the luminescent nanofeatures of the recorded spots (Extended Data Fig. 7b). Images featuring densely arranged recorded spots of a panda pattern are presented in Extended Data Fig. 7c–e, which illustrate the technique's ability to resolve intricate and complex patterns at the nanoscale level. The proof-of-concept for nanoscale ODS on a commercial base disk is shown in Extended Data Fig. 8a–d.

Characterizations of emission spectrum, time-resolved photoluminescence and Raman spectroscopic measurements were performed to illustrate the AIE mechanism. First, we used an integrated fluorescence lifetime imaging microscopy (FLIM) confocal platform (STELLARIS 8 STED FALCON, Leica) to characterize the fluorescence lifetime of the AIE-DDPR film. In the system, a 480-nm pulsed laser beam (repetition rate 80 MHz; pulse width 5 ps) was focused by an oil-immersion objective (UPlanSApo, Olympus; $\times 100$, numerical aperture 1.4) onto the sample. Subsequently, the photoluminescence emitted from the sample was collected by the same objective. The FLIM measurement was made using a confocal scan head equipped with field-programmable gate array electronics and employed pulsed laser excitation and fast, spectral single-photon counting detectors. Photon arrival times were determined from the difference between the detection-pulse and laser-pulse arrival times recorded at count rates that are typically used for confocal imaging. The fast FLIM image and corresponding FLIM histogram are shown in Extended Data Fig. 8e,f. Overall decay curves (Fig. 3d) were fitted to the sums of the following exponential decay components using equation (15), and the average lifetimes of a bi-exponential decay ($n = 2$) were calculated using equation (16).

$$y(t) = \sum_{i=0}^{n-1} A[i] e^{-\frac{t}{\tau(i)}} + Bkgr \quad (n=2) \quad (15)$$

$$\tau_{\text{AvAmp}} = \frac{\sum_{k=0}^{n-1} A[k] \tau[k]}{A_{\text{Sum}}} \quad (n=2) \quad (16)$$

where A is the amplitudes and exponential pre-factors, $Bkgr$ is the tail offset which is the correction for background of afterpulsing, dark counts and environmental light. τ_{AvAmp} is the amplitude weighted average mean decay time. A_{Sum} is the sum of fluorescence intensity for all components at time zero. The radiative and non-radiative decay rates were calculated from the average lifetimes and QYs.

$$k_r = \text{QY}/\tau \quad (17)$$

$$k_{\text{nr}} = (1 - \text{QY})/\tau \quad (18)$$

Next, we adopted confocal Raman spectroscopy to probe the microstructures and thus measure the degree of polymerization of the AIE-DDPR film in the second and third states using the 515-nm femtosecond laser beam at different writing powers. The degree of polymerization can be quantified by the degree of conversion. A high degree of conversion corresponds to a high degree of polymerization and a strong film. The degree of conversion was estimated by detecting the Raman spectrum peak at approximately $1,638 \text{ cm}^{-1}$, which corresponds to the stretching vibration of the carbon–carbon double bond (C=C)⁴⁹. During the polymerization, the intensity of the peak at approximately $1,638 \text{ cm}^{-1}$ decreased because the C=C was reduced to a carbon–carbon single bond (C–C)⁴⁹. Raman spectra were acquired by placing samples in a laser confocal Raman spectrometer (RAMANtouch) equipped with a 785-nm laser with an incident power of 30 mW. Next, the system was calibrated using the peak for silicon at 520.5 cm^{-1} , and then the laser beam was focused on a sample to a size of $1.2 \mu\text{m}$ by an objective (UPlan ELWD, $\times 100$, numerical aperture 0.8, Nikon). The laser exposure time was 15 s. The acquired spectra were normalized to the carbonyl (C=O) peak at $1,720 \text{ cm}^{-1}$ because the number of C=O groups in the film was unaffected by polymerization. The degree of conversion was calculated from the Raman spectral data as follows:

$$DC = [1 - \frac{A_{\text{C=C}}/A_{\text{C=O}}}{A'_{\text{C=C}}/A'_{\text{C=O}}}] \times 100 \quad (19)$$

where $A_{\text{C=C}}$ and $A_{\text{C=O}}$ are the integrated intensities of the C=C peak and the C=O peak, respectively, for the AIE-DDPR exposed to ultraviolet light and the 515-nm femtosecond laser beam with different writing powers, and $A'_{\text{C=C}}$ and $A'_{\text{C=O}}$ are the intensities of the same peaks for the AIE-DDPR in the colloidal state. The degree of conversion values calculated from the Raman spectra were 35.5%, 39.6%, 41.2%, 43.9%, 46.1% and 47.9% for the various powers of the 515-nm femtosecond laser beam, that is, 0 mW (that is, only ultraviolet curing for the second state) and 0.3–1.5 mW (that is, the third state). At writing powers of 0.5 mW and 1.5 mW, the degree of conversion values of the third state were 5.7% and 12.4% greater, respectively, than the degree of conversion values of the second state, which means that the degree of polymerization was much higher in the third state than in the second state.

The degree of conversion values, lifetimes, QYs, and radiative and non-radiative decay rates of the recorded areas at different writing powers of the 515-nm femtosecond laser beam (that is, the third state) and the area with only ultraviolet curing (that is, the second state) are summarized in Extended Data Table 2.

Lifetime and durability of ODS based on the AIE-DDPR film

We conducted an accelerated-ageing test to calculate the lifetime and durability of room-temperature ODS in the AIE-DDPR film. We applied the Arrhenius method, which considers only the temperature stress condition, and thus the time-to-failure was assumed to be governed by the following Arrhenius-model formula:

$$k = A e^{-\frac{E_a}{RT}} \quad (20)$$

where E_a is the activation energy, RT is the average kinetic energy, R is the gas constant, T is temperate in kelvin and A is a pre-exponential factor. This equation can be rewritten in a non-exponential form. That is, taking the logarithms of both sides yields

$$\ln k = \ln A - \frac{E_a}{RT} \quad (21)$$

Thus, $\ln(k)$ and $1/T$ fulfil a linear relationship. The time-to-failure k was determined by evaluating the fluorescence attenuation of the recorded spots versus the incubation time of the accelerated-ageing conditions (130 °C and 120 °C). At 130 °C, the incubation times used

were 6 h, 10 h, 12 h, 13 h, 15 h and 18 h, and the scanning fluorescence and white-light microscopic images are shown in Extended Data Fig. 9a,c. At 120 °C, the incubation times used were 15 h, 16 h, 20 h, 24 h, 26 h and 27 h, and the scanning fluorescence and white-light microscopic images are shown in Extended Data Fig. 9b,d. $k = 1/\tau$, where τ is the lifetime of the recording structure when the fluorescence completely disappears. $\tau = 12$ h and $\tau = 26$ h at 130 °C and 120 °C, respectively. From our experimental data, we deduced that the lifetime of ODS in the AIE-DDPR film at room temperature is 41 years.

Data availability

The data that support the findings of this study are available at <https://doi.org/10.57760/scencedb.13342> (ref. 50). Source data are provided with this paper.

Code availability

The MATLAB code used in this study is available at <https://doi.org/10.57760/scencedb.13342> (ref. 50).

41. Chi, T. et al. Substituted thioxanthone-based photoinitiators for efficient two-photon direct laser writing polymerization with two-color resolution. *ACS Appl. Polym. Mater.* **3**, 1426–1435 (2021).
42. Harke, B. et al. Polymerization inhibition by triplet state absorption for nanoscale lithography. *Adv. Mater.* **25**, 904–909 (2013).
43. Fischer, J. et al. Exploring the mechanisms in sted-enhanced direct laser writing. *Adv. Opt. Mater.* **3**, 221–232 (2015).
44. Gan, Z., Cao, Y., Jia, B. & Gu, M. Dynamic modeling of superresolution photoinduced-inhibition nanolithography. *Opt. Express* **20**, 16871–16879 (2012).
45. Gleeson, M. R. & Sheridan, J. T. Nonlocal photopolymerization kinetics including multiple termination mechanisms and dark reactions. Part I. Modeling. *J. Opt. Soc. Am. B* **26**, 1736–1745 (2009).
46. Gleeson, M. R., Liu, S., McLeod, R. R. & Sheridan, J. T. Nonlocal photopolymerization kinetics including multiple termination mechanisms and dark reactions. Part II. Experimental validation. *J. Opt. Soc. Am. B* **26**, 1746–1754 (2009).
47. Amirzadeh, G. & Schnabel, W. On the photoinitiation of free radical polymerization-laser flash photolysis investigations on thioxanthone derivatives. *Macromol. Chem. Phys.* **182**, 2821–2835 (1981).
48. Ye, Y. et al. Monolayer excitonic laser. *Nat. Photon.* **9**, 733–737 (2015).
49. Diamantopoulou, M., Karathanasopoulos, N. & Mohr, D. Stress-strain response of polymers made through two-photon lithography: micro-scale experiments and neural network modeling. *Addit. Manuf.* **47**, 102266 (2021).
50. Zhao, M. et al. A 3D nanoscale optical disc memory with petabit capacity. *Science Data Bank* <https://doi.org/10.57760/scencedb.13342> (2023).

Acknowledgements J.W. acknowledges the financial support from the National Natural Science Foundation of China (NSFC, project no. 62175153). M.G. acknowledges the support from the Science and Technology Commission of Shanghai Municipality (project no. 21DZ1100500) and the Shanghai Municipal Science and Technology Major Project. M.G., J.W. and H.R. acknowledge the financial support from the Shanghai Municipal Science and Technology Commission Innovation Action Plan (project no. 18DZ1100400). M.G. and H.R. acknowledge the financial support from the National Key R&D Program of China (project no. 2021YFB2802000). Y.-W.Z. acknowledges the support from the National Natural Science Foundation of China (NSFC, project no. 21925112). X.W. acknowledges the support from the National Natural Science Foundation of China (NSFC, project no. 62027824). We thank Z. Gan from Huazhong University of Science and Technology for the adjustment of the optical writing set-up. We thank F. Liu from the Integrated Laser Microscopy System and Computation System at the National Facility for Protein Science in Shanghai (NFPS), Zhangjiang Lab for providing usage and technical support for the STED microscope. We thank H. H. Li and E. K. Zhang from Leica Microsystems (Shanghai) Trading Company Ltd for time-resolved photoluminescence detection and emission spectrum measurement. We thank D. Y. Lei and S. Y. Jin from the City University of Hong Kong for the discussion of the measurement of fluorescence lifetime in microscale. We thank H. X. Xu from Wuhan University, and D. Pan and C. J. Zhang from East China Normal University for helping with the Raman measurement in microscale. We thank T. C. Tang from the University of Shanghai for Science and Technology for data baseline cutting in the Raman measurement. We thank W. X. Cao from the Shanghai Institute of Optics and Fine Mechanics, Chinese Academy of Sciences for joining the shelf lifetime measurement of the sample.

Author contributions M.G., H.R. and J.W. conceived the original concept and initiated the work. J.W., M.Z. and Q.H. performed the theoretical analysis and conducted the simulation. M.Z. and J.W. synthesized the material. M.Z., J.W. and H.R. developed the set-up and performed the measurements. J.W., M.Z., H.R., Y.-W.Z. and M.G. analysed the data and explained the mechanism. M.G., J.W., H.R., M.Z. and Y.-W.Z. discussed the results. J.W., M.G., M.Z., X.W. and H.R. wrote the paper and all authors reviewed the paper.

Competing interests The authors declare no competing interests.

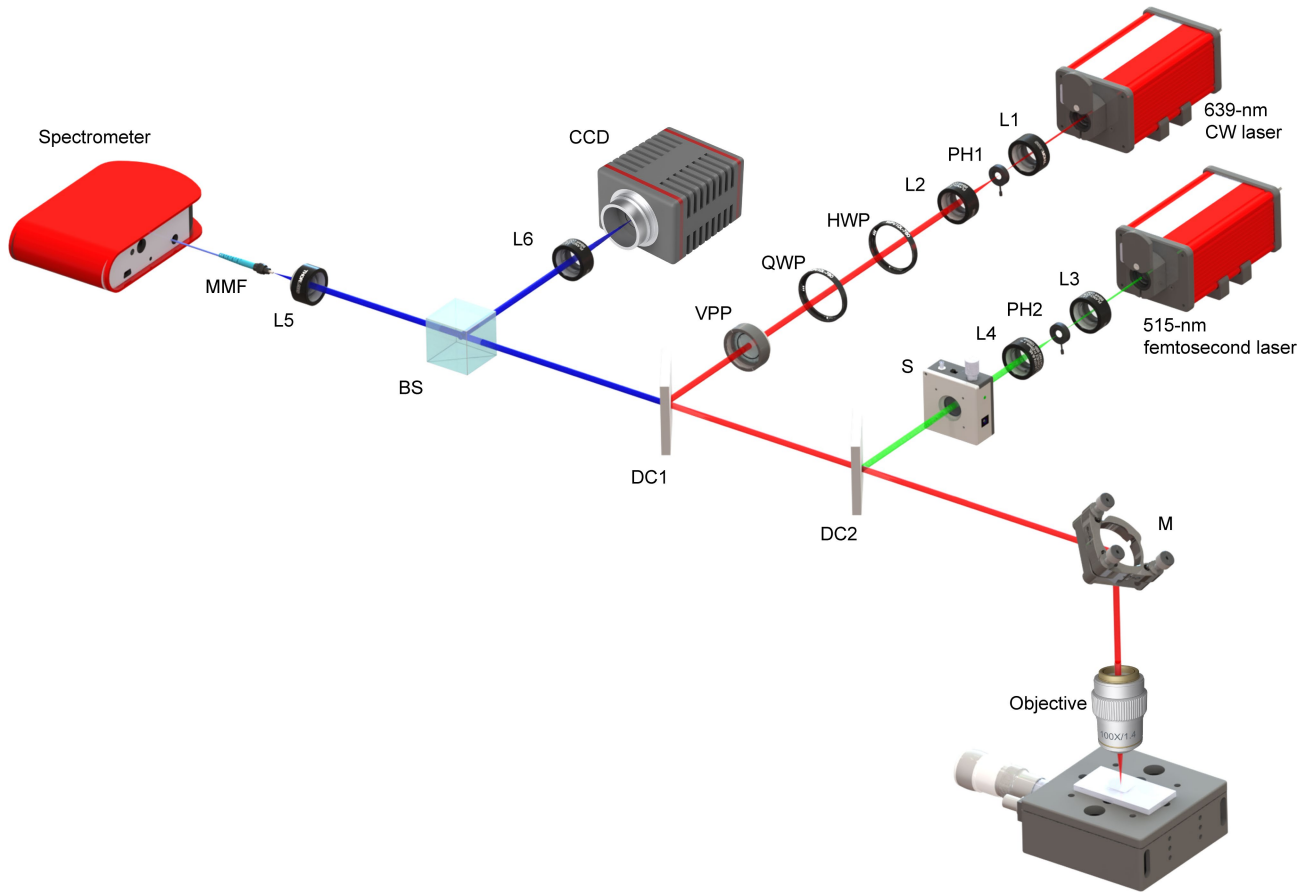
Additional information

Supplementary information The online version contains supplementary material available at <https://doi.org/10.1038/s41586-023-06980-y>.

Correspondence and requests for materials should be addressed to Jing Wen, Hao Ruan or Min Gu.

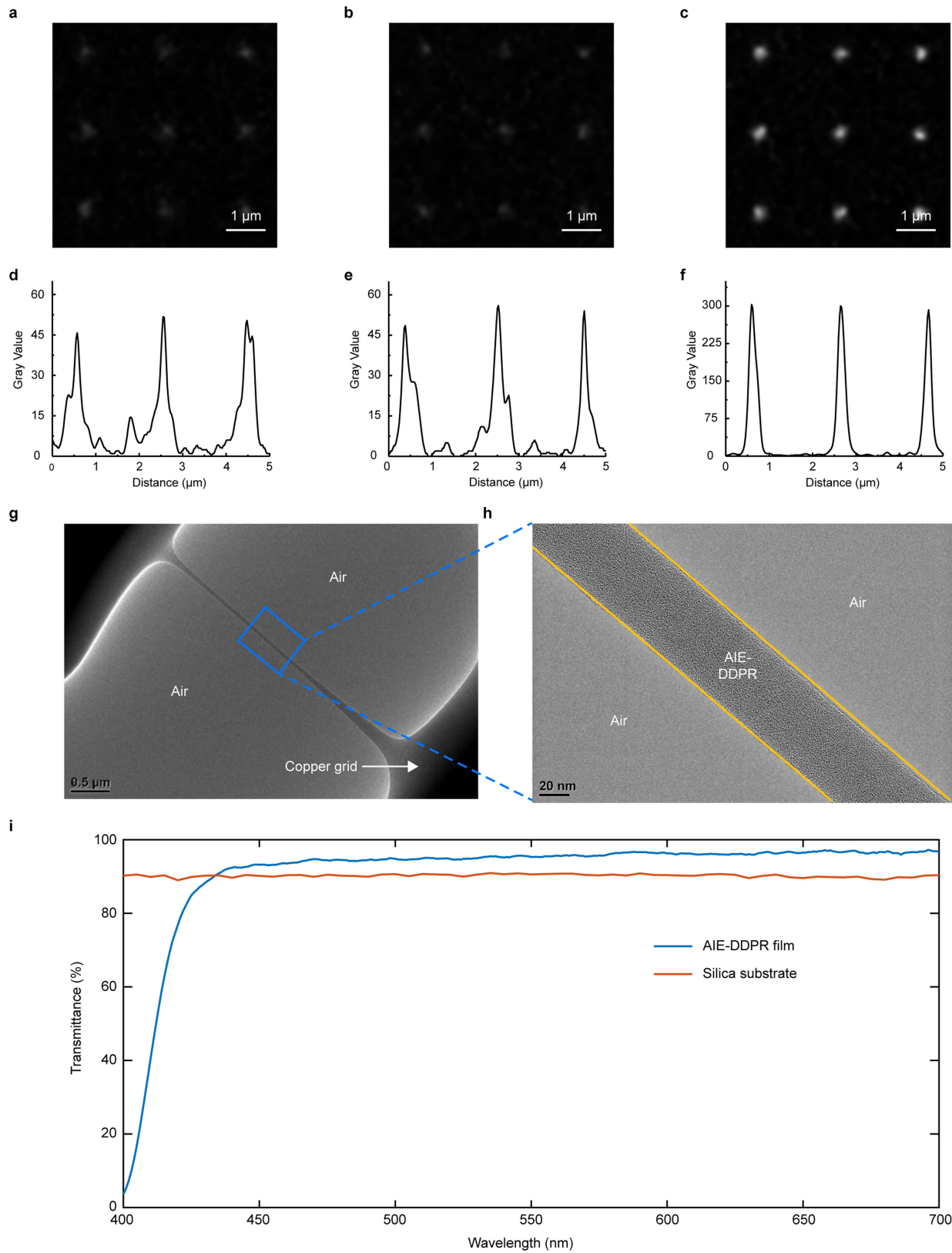
Peer review information *Nature* thanks Peter Kazansky, Xiewen Wen and the other, anonymous, reviewer(s) for their contribution to the peer review of this work.

Reprints and permissions information is available at <http://www.nature.com/reprints>.



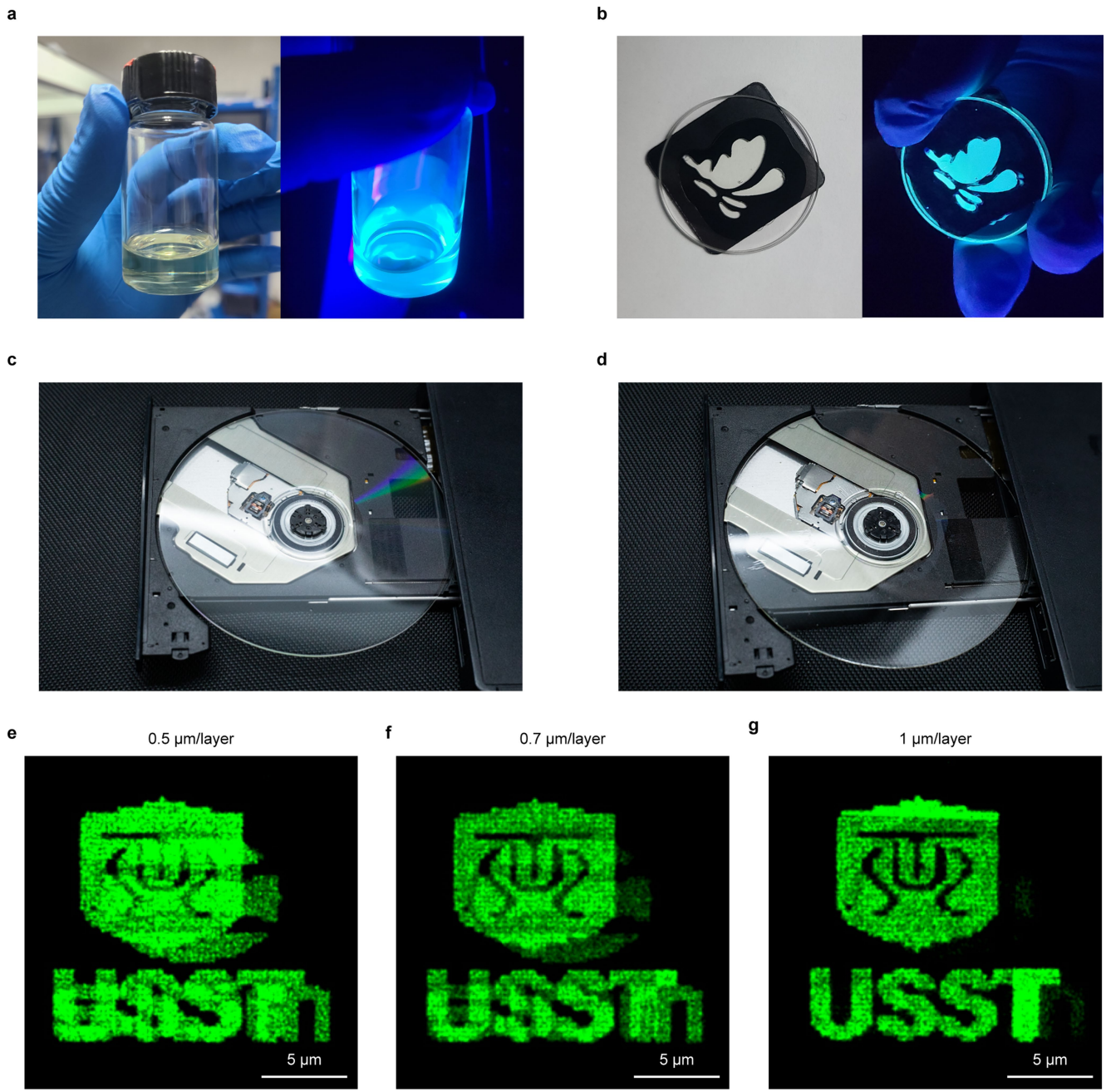
Extended Data Fig. 1 | Optical setup of dual-beam volumetric nanoscale writing. L1, L2, L3, and L4, collimation lenses; L5, collection lens; L6, tube lens; PH1 and PH2, pinholes; HWP, half-wave plate; QWP, quarter-wave plate; VPP, vortex-phase plate; DC1 and DC2, dichroic filters; S, electronic shutter;

M, mirror; BS, beam-splitter; MMF, multi-mode fibre; and CCD, charged coupled device. Source images of the optical components provided courtesy of Thorlabs, Inc.



Extended Data Fig. 2 | Summary of an aggregation-induced emission dye-doped photoresist (AIE-DDPR) film. **a–c**, Fluorescence images of the ODS medium doped with tetraphenylethene (**a**), no AIEgens (**b**) and hexaphenylsilole (**c**) obtained by the Leica microscope. **d–f**, Intensity profiles (**d**, **e**) and (**f**) are

extracted from (**a–c**). **g**, Transmission electron microscopy image of a cured AIE-DDPR film. **h**, Expansion of the blue-boxed area in (**g**). **i**, Transmittance of a cured AIE-DDPR film with a thickness of 130 μm (blue line) and a pure silica substrate with a thickness of 980 μm (red line).



Extended Data Fig. 3 | Aggregation-induced emission dye-doped photoresist (AIE-DDPR) recording medium in colloidal and solid states and fluorescence images of the volumetric writing with different layer spacings.
a, AIE-DDPR in the colloidal state under white-light illumination (left) and ultraviolet (UV)-light illumination (right). **b**, Cured spin-coated AIE-DDPR film

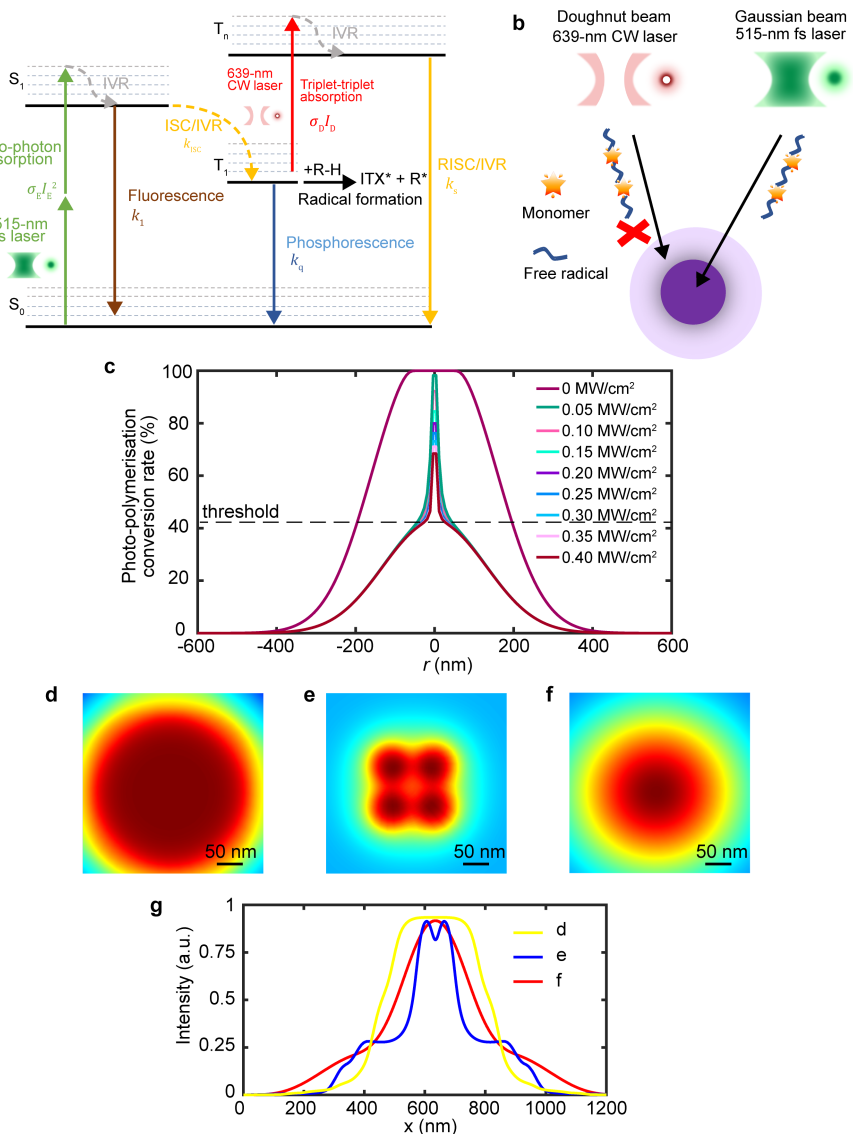
under white-light illumination (left) and UV-light illumination (right). **c**, Base disc comprising the substrate. **d**, Disc spin-coated with a film of AIE-DDPR that has been cured (a blank disc yet to be written with information). **e–g**, There was strong cross-talk of the signal when the layer spacing was 0.5 μm (e) or 0.7 μm (f), and no cross-talk of the signal when the layer spacing was 1 μm (g).

a Binary numbers of the encoded image in Figure 2e

b Binary numbers of the recalled image in Figure 2e

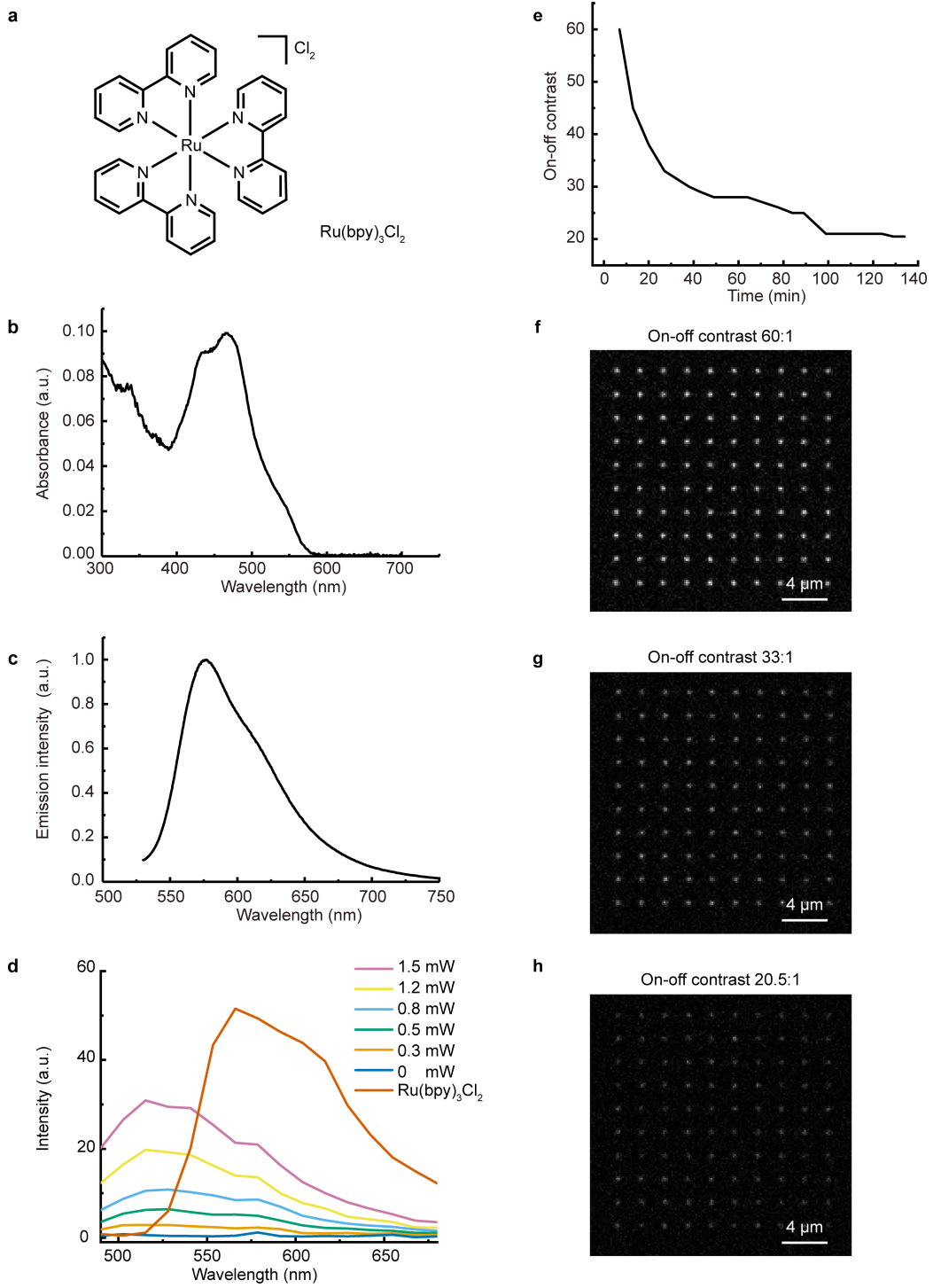
Extended Data Fig. 4 | Binary bits of the encoded image (a) and the recalled image (b) in Fig. 2e. In a, '1' and '0' represent the writing beam being 'on' and 'off' which are controlled by the electronic shutter in Extended Data Fig. 1.

In **b**, '1' and '0' represent the fluorescent signal from the recording medium being 'on' and 'off'.



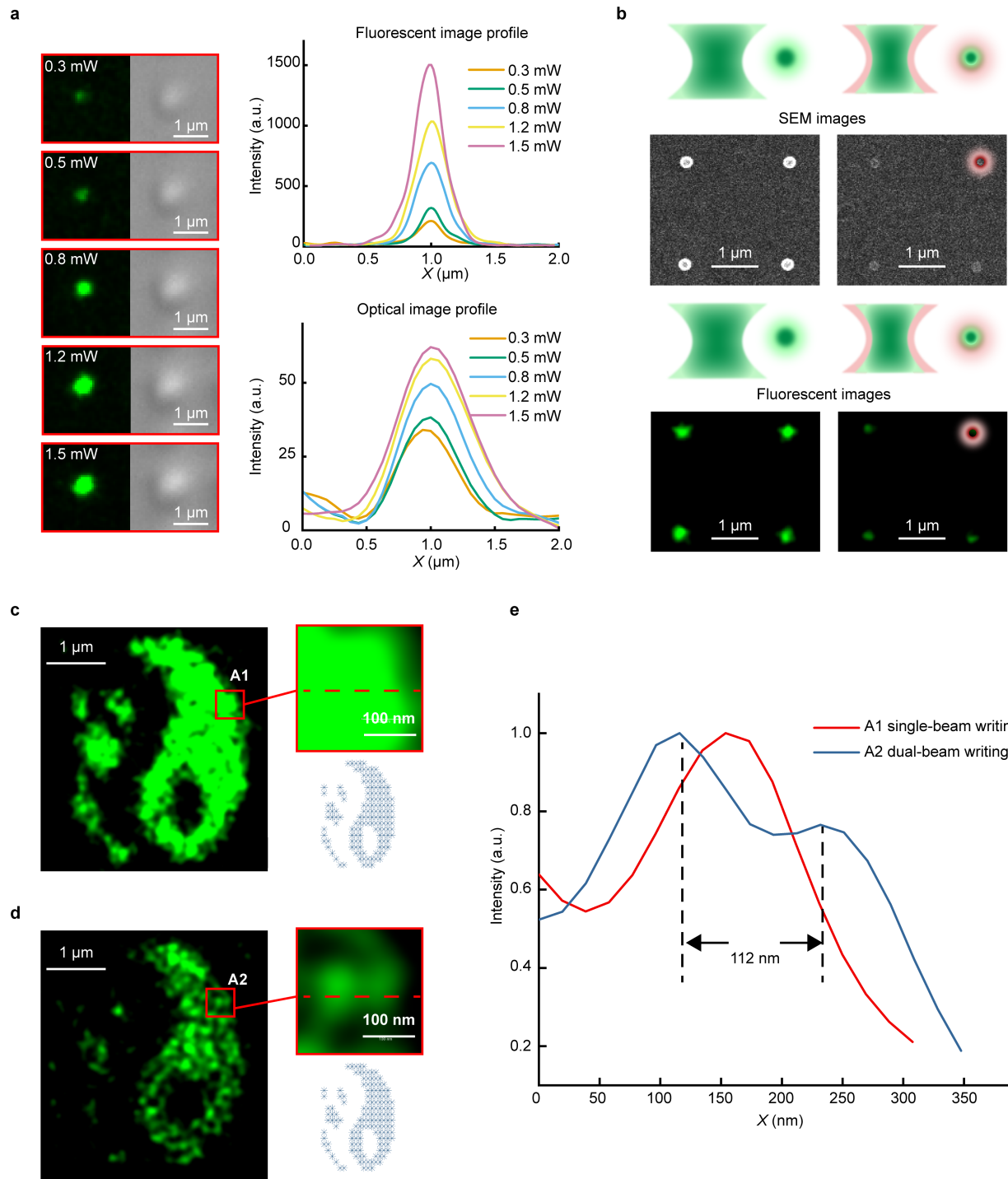
Extended Data Fig. 5 | Schematic illustration of the writing principle of volumetric nanoscale ODS and simulations. **a.** Jablonski diagram of 2-isopropylthioxanthone photoinitiators for the explanation of polymerization by two-photon absorption and depolymerization by triplet–triplet absorption. The green arrows indicate the absorption of the two photons, the brown arrow indicates the radiative relaxation of the fluorescence, the blue arrow indicates the radiative relaxation of the phosphorescence, the grey dashed arrow indicates intramolecular vibrational redistribution (IVR), the red arrow indicates triplet–triplet absorption, the yellow arrows indicate intersystem crossing (ISC)/IVR (dashed arrow) or reverse ISC/IVR (solid arrow), and the black arrow indicates radical formation. The energy levels are not to scale. The solid horizontal lines indicate nonvibrational electronic states whereas the dashed horizontal lines indicate vibrationally excited electronic states. **b.** Principle of dual-beam

nanoscale optical writing. A 515-nm femtosecond Gaussian laser beam initiates polymerization in a medium via two-photon absorption, and a 639-nm CW doughnut-shaped laser beam then deactivates locally the polymerization at the periphery of the focus, which reduces the polymerization volume to the subdiffractive level. **c.** Simulated profiles of photo-polymerization conversion rate versus deactivating intensity in a dual-beam writing process. The threshold was set to 42%, with the area above 42% representing the third state in Fig. 3, and the area below 42% representing the second state in Fig. 3. **d** and **e**, Simulated superresolution STED images of a 4×4 pattern formed by the 515-nm femtosecond writing laser beam without (**d**) and with (**e**) subsequent application of the 639-nm deactivating beam. **f**, Simulated confocal image of the pattern formed by the dual-beam writing configuration. **g**, Intensity profiles extracted from (**d–f**).



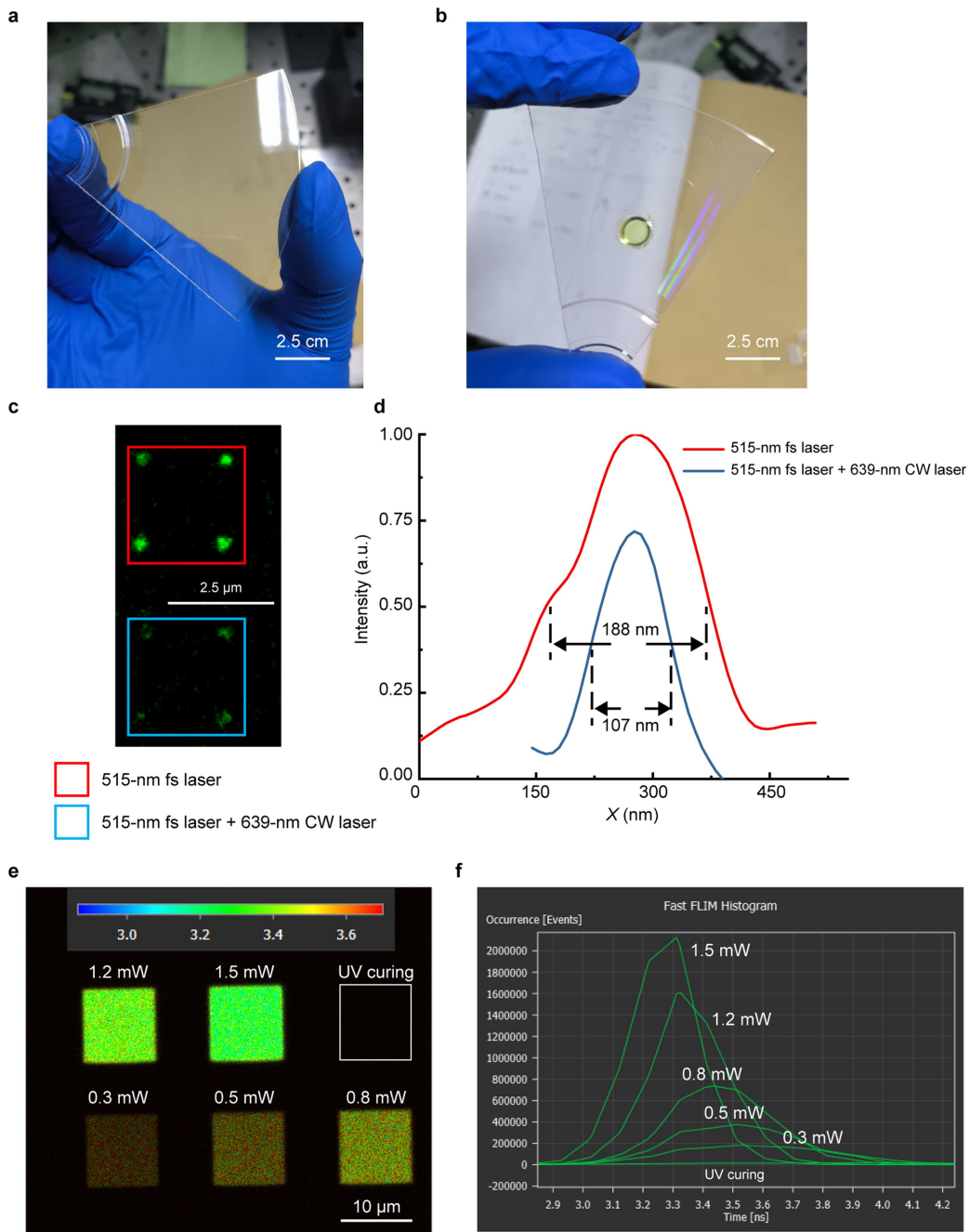
Extended Data Fig. 6 | Properties of the standard sample of $\text{Ru}(\text{bpy})_3\text{Cl}_2$ thin film and the aggregation-induced emission dye-doped photoresist (AIE-DDPR) film for characterization of QYs and fluorescence on-off contrast of the recorded spots. **a–c.** (a) Chemical formula. The QY of $\text{Ru}(\text{bpy})_3\text{Cl}_2$ thin film is 7.3% which is calculated from the absorbance (b) and the fluorescence emission intensity (c) at an excitation wavelength $\lambda = 480$ nm. **d.** Fluorescence intensity of the AIE-DDPR film at an excitation wavelength

$\lambda = 480$ nm before exposure to the femtosecond laser (0 mW, i.e., the second state in Fig. 3) and after exposure to the 515-nm femtosecond laser with various writing powers, i.e., 0.3–1.5 mW (i.e., the third state in Fig. 3), and the standard sample of $\text{Ru}(\text{bpy})_3\text{Cl}_2$ thin film. **e.** Photobleaching: fluorescence on–off contrast of a recorded spot probed by irradiation with a 480-nm pulsed laser. **f–h.** Fluorescence image obtained at 7 min (f), 27 min (g), and 134 min (h) after the beginning of excitation.



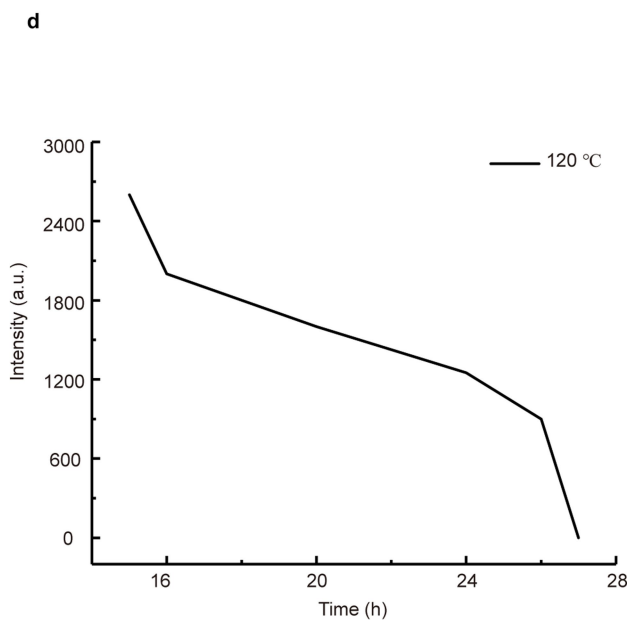
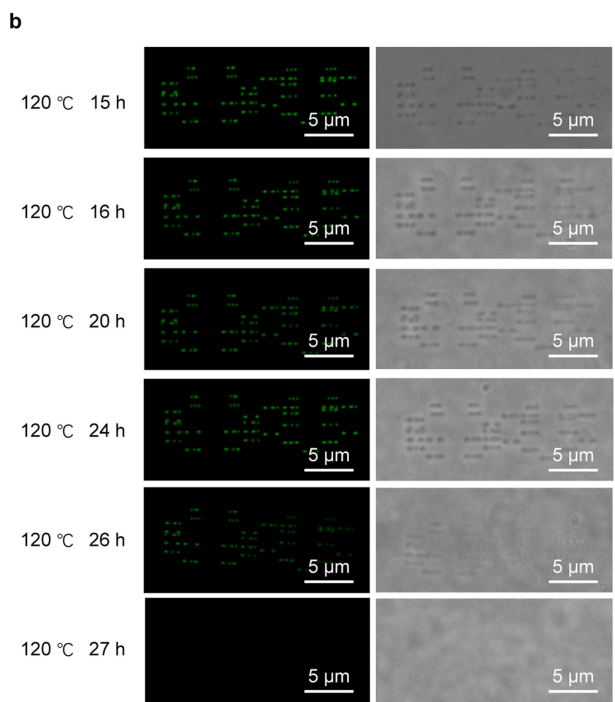
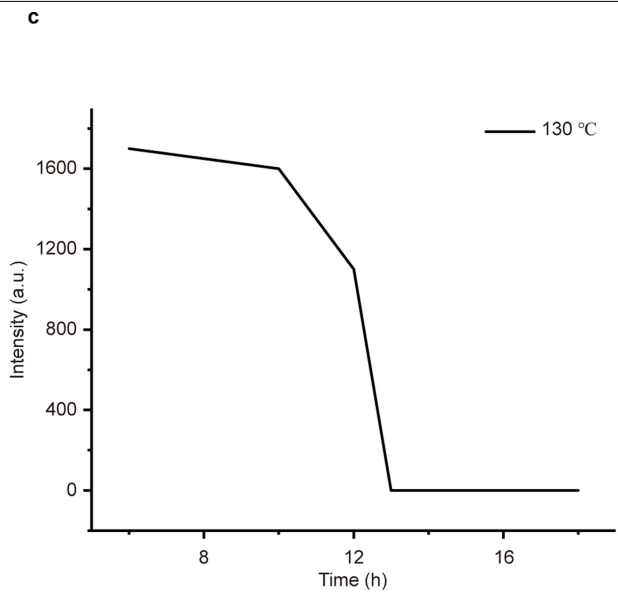
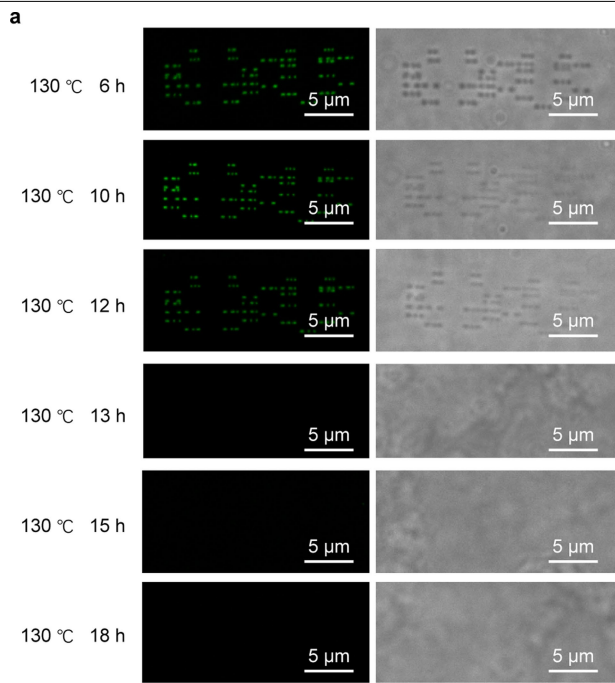
Extended Data Fig. 7 | Comparison of fluorescence images and aggregation sizes of the recorded spots with the 515-nm femtosecond Gaussian laser beam only and dual-beam writing. **a**, Fluorescence and optical images of the recorded spots at different writing powers of the 515-nm femtosecond laser beam, as measured in the optical path. **b**, Scanning electron microscopy (SEM) images and fluorescent images of diffraction-limited spots recorded by the 515-nm femtosecond Gaussian laser beam only and subdiffractive spots recorded by the dual-beam writing configuration. Scale bar: 1 μ m.

c and **d**, Superresolution imaging of densely arranged spots of a panda yin-yang pattern. Superresolution STED-image readouts of the recording patterns formed by the 515-nm femtosecond writing laser beam without (**c**) and with (**d**) subsequent application of the 639-nm CW deactivating beam. Insets: Magnified images of 1×2 recording spots and the original panda yin-yang pattern. **e**, Intensity profiles extracted from the areas marked with the dashed lines in the magnified images in (**c**) and (**d**). The panda yin-yang pattern is discretized to a 21×21 dot matrix with a spacing of 112 nm.



Extended Data Fig. 8 | ODS on optical base disc and fluorescence lifetime imaging of the recording areas. **a**, A base disc comprising only substrate. **b**, A disc with a transparent-yellow circle of the aggregation-induced emission dye-doped photoresist (AIE-DDPR) that has been subsequently cured. **c**, Superresolution imaging of recording spots formed by the 515-nm femtosecond writing beam without and with the application of the 639-nm CW deactivating beam. **d**, Intensity profiles extracted from the areas marked with the white dashed lines in the red and blue boxes in (c). The recording-spot sizes were 107 nm and 188 nm for dual-beam writing and single-beam writing, respectively. We had to scan a portion of the optical disc as the scanning stage could not accommodate a whole disc. **e** and **f**, Scanning fast fluorescence lifetime imaging microscopy (FLIM) image (e) and the corresponding FLIM histogram (f) for the recorded areas at different writing powers of the 515-nm femtosecond laser beam (the third state) and the background area with only ultraviolet curing (the second state). The recording areas were written at a scan speed of 2.5 μ m/s and comprised parallel lines with a line spacing of 300 nm.

188 nm for dual-beam writing and single-beam writing, respectively. We had to scan a portion of the optical disc as the scanning stage could not accommodate a whole disc. **e** and **f**, Scanning fast fluorescence lifetime imaging microscopy (FLIM) image (e) and the corresponding FLIM histogram (f) for the recorded areas at different writing powers of the 515-nm femtosecond laser beam (the third state) and the background area with only ultraviolet curing (the second state). The recording areas were written at a scan speed of 2.5 μ m/s and comprised parallel lines with a line spacing of 300 nm.



Extended Data Fig. 9 | Lifetime and durability test of ODS. **a** and **b**, Scanning fluorescence and white-light microscopic images of the recorded spots for the temperature stress condition of 130 °C and 120 °C. The time is incubation time.

c and **d**, The intensities for different incubation times (**c**) and (**d**) were extracted from the fluorescence images (**a**) and (**b**).

Extended Data Table 1 | Recording resolutions and capacities of different storage systems

Material	Mechanism	Calculated capacity/ DVD-sized disc area (1GB=8Gb)	Spot size	Pitch size	Areal density	Number of experimentally realized recording layers
Our AIE-DDPR	Dual beam writing based on triplet-triplet absorption (TTA) and stimulated depletion emission (STED) inspired reading	One side: 800 Tb (100 layers) Double sides: 1.6 Pb (200 layers)	54 nm	70 nm	One side: 13 Tb/in ² (100 layers) Double side: 26 Tb/in ² (200 layers)	100/one side 200/double sides
Gold nanorods. Ref. ⁷	5D wavelength and polarization multiplexed states	12.8 Tb (10 layers)	750 nm	1.33 μ m	210 Gb/in ² (10 layers)	10
Reversibly switchable enhanced green fluorescent protein (rsEGFP). Ref. ²⁷	Reversible, saturable/switchable optical fluorescence transition (RESOLFT) inspired writing and reading	1 Tb (1 layer)	/	200 nm	16 Gb/in ² (1 layer)	1
Lanthanide-doped upconversion nanoparticles (UCNPs) and graphene oxide (GO). Ref. ²⁸	Resonance energy transfer (RET) on GO-conjugated UCNPs	2.5 Tb (1 layer)	50 nm	125 nm	41 Gb/in ² (1 layer)	1
Silica glass. Ref. ¹¹	Multi-layer 5D optical disc based on birefringent modification	2.8 Tb (100 layers)	/	2 μ m	46 Gb/in ² (100 layers)	100
Commercial Blue-ray disc. Ref. ²	Reflections of light on pitches and lands	300 Gb (1 layer) 1.8 Tb (6 layers) (3 layers on one side; 6 layers on double sides)	/	320 nm	4.9 Gb/in ² (1 layer) 29 Gb/in ² (6 layers)	3/one side 6/double sides
HDDs. Ref. ³² (Exos X20 20TB, Seagate 2021, USA) (Ultrastar DC HC560 20TB, WD 2021, USA)	Magnetic storage	/	/	/	1.1 Tb/in ²	1

Various mechanisms, calculated capacities for a DVD-sized disc area, minimum sizes of the recording spots, pitch sizes (i.e., minimum distances of the neighboring spots), areal densities and numbers of experimentally realized recording layers for different recording materials.

Article

Extended Data Table 2 | Degree of conversion (DC) values, mean lifetimes, quantum yields (QYs), nonradiative and radiative decay rates of the recorded areas at different writing powers of the 515-nm femtosecond laser beam (i.e., the third state), and the area with only ultraviolet curing (i.e., the second state)

	DC	τ (ns) (mean lifetime)	QY	k_{nr} (s ⁻¹)	k_r (s ⁻¹)
The second state	35.5%	6.605	0.014	1.493×10^8	2.120×10^6
The third state power of 515-nm fs laser					
0.3 mW	39.6%	3.778	0.053	2.507×10^8	1.403×10^7
0.5 mW	41.2%	3.269	0.112	2.716×10^8	3.426×10^7
0.8 mW	43.9%	3.090	0.191	2.619×10^8	6.172×10^7
1.2 mW	46.1%	2.877	0.325	2.347×10^8	1.129×10^8
1.5 mW	47.9%	2.708	0.511	1.807×10^8	1.886×10^8

When the writing power of the 515-nm femtosecond laser beam increases, the corresponding DC value and QY increases which means a higher degree of polymerization (a stronger film) emits brighter light. This is in accordance with an increasing radiative decay rate and a decreasing nonradiative decay rate, which were calculated from the average lifetimes and QYs.